CrossMark

JM PAPERS

Towards a consistent lattice Boltzmann model for two-phase fluids

S.A. Hosseini[1], B. Dorschner[1] and I.V. Karlin[1],†

[1]Department of Mechanical and Process Engineering, ETH Zurich, 8092 Zurich, Switzerland

We revisit the construction of discrete kinetic models for single-component isothermal two-phase flows. Starting from a kinetic model for a non-ideal fluid, we show that, under conventional scaling, the Navier–Stokes equations with a non-ideal equation of state are recovered in the hydrodynamic limit. A scaling based on the smallness of velocity increments is then introduced, which recovers the full Navier–Stokes–Korteweg equations. The proposed model is realized on a standard lattice and validated on a variety of benchmarks. Through a detailed study of thermodynamic properties including co-existence densities, surface tension, Tolman length and sound speed, we show thermodynamic consistency, well-posedness and convergence of the proposed model. Furthermore, hydrodynamic consistency is demonstrated by verification of Galilean invariance of the dissipation rate of shear and normal modes and the study of visco-capillary coupling effects. Finally, the model is validated on dynamic test cases in three dimensions with complex geometries and large density ratios such as drop impact on textured surfaces and mercury drops coalescence.

Key words: multiphase flow, kinetic theory

1. Introduction

Multi-phase flows are omnipresent in science and technology. From micro-droplets coalescing in clouds to solidification or melting of alloys and diesel droplets evaporation and subsequent combustion, all involve multiple interacting phases and moving interfaces. This ubiquity fuelled wide efforts focused on the development of predictive mathematical models and numerical tools for multi-phase flows. While significant attention has been focused on sharp interface methods requiring efficient tracking of the evolving and deforming interfaces, and imposing jump conditions (Scardovelli & Zaleski 1999;

† Email address for correspondence: ikarlin@ethz.ch

953 A4-1

Sethian & Smereka 2003; Prosperetti & Tryggvason 2009; Popinet 2018), the ever-growing range of temperatures and pressures involved in typical systems of interest is making thermodynamic consistency of the computational models essential. For instance, dramatically different thermodynamic regimes are encountered in diesel engines during the compression phase, in aeronautical engines during take-off, while most rocket engines operate in trans- and super-critical regimes, where the interface thickness becomes comparable to the flow scales. Nucleation and cavitation are yet another example, where the sharp interface limit does not hold and modifications to the classical nucleation theory (Debenedetti 1997), related to curvature-dependence of the surface tension, are required. In such cases, an accurate account of the non-ideality of the fluid, including a finite interface thickness, is crucial for predictive numerical simulations of the flow physics. At a macroscopic level, a prime example for thermodynamics of non-ideal fluids is the second-gradient theory, first introduced by van der Waals for single-component fluids (van der Waals 1894), leading to the Navier–Stokes equations supplemented with the Korteweg stress tensor (Korteweg 1901), and is a starting point for numerical methods known as the diffuse interface approach (Anderson, McFadden & Wheeler 1998). Additionally, extension of the Boltzmann equation to dense gases within the Enskog hard-sphere collision model (Enskog 1921) and the Vlasov mean-field approximation (Vlasov 1961) provides a kinetic-theory basis for the dynamics of a non-ideal fluid (Chapman & Cowling 1939).

Since the pioneering work of Shan & Chen (1993), the lattice Boltzmann method (LBM) has gained popularity as a viable numerical tool targeting the hydrodynamic regime of multi-phase flows. Despite their popularity and wide usage, most multi-phase models for LBM, apart from a limited number of studies (He, Shan & Doolen 1998; Martys 2001, 1999, 2006; He & Doolen 2002), lack a clear kinetic-theory thermodynamic framework and/or well-defined target continuum thermodynamics. For instance, despite active development and research, the so-called pseudo-potential lattice Boltzmann models lack a clear and consistent continuous kinetic model, scaling law recovering the full target macroscopic system and continuum level free energy functional (Sbragaglia *et al.* 2009). Thorough analyses of the bulk thermodynamic and interface properties of the models (especially near the critical state) are also very scarce. Furthermore, ever since their inception, such models have continuously struggled with larger density ratio simulations achieving at best, via different strategies, ratios of the order of 10^3, as reflected by a number of recent reviews (Chen *et al.* 2014; Li *et al.* 2016).

In this paper, we revisit the construction of the lattice Boltzmann model for isothermal two-phase flows. We propose a flexible kinetic framework for dense fluids with non-ideal equations of states. Using the lattice Boltzmann method discretization strategy, and under proper scaling, the model is shown to recover the full Navier–Stokes–Korteweg system of equations. Through a detailed study of the thermodynamic properties, the model is shown to be well posed and convergent to the capillary fluid thermodynamics. The well-posedness of the model and proper consideration of the proposed scaling is shown to guarantee recovery of the hydrodynamic-scale dynamics both at very large density ratio and near critical point.

The outline is as follows: we begin in § 2.1 with a summary of the second-gradient theory due to van der Waals (1894) and Korteweg (1901). In § 2.2, following a more microscopic approach, we consider a class of kinetic models suitable for a non-ideal fluid. We proceed in § 2.3 with a scaling assumption of small flow velocity increments which leads to a lattice Bhatnagar–Gross–Krook (LBGK) equation with a new realization of the non-local force that guarantees consistency with Korteweg's stress.

Thermodynamics of the LBGK model is validated in § 3. In §§ 3.1 and 3.2, we demonstrate convergence of vapour–liquid coexistence to the thermodynamic Maxwell construction via the principle of corresponding states (Guggenheim 1945), independently of the equation of state and for liquid–vapour density ratios up to at least $\sim 10^{11}$. The remainder of the paper is based on the van der Waals equation of state. In § 3.3, we show that the surface tension in the present LBGK model obeys a temperature scaling in excellent agreement with the theory. After verifying that the proposed model allows for choosing surface tension independently of the density ratio in § 3.4, we show in § 3.5 that it is also consistent with Gibbs' theory of dividing surfaces (Gibbs 1874). Simulations presented in § 3.5 reveal a generalized Laplace law and uncover the effect of curvature on the surface tension, in agreement with the theory by Tolman (1949). Finally, in § 3.6, we show that the interface width scales with the temperature in accord with van der Waals theory.

We turn to probing hydrodynamic features of our model in § 4. In § 4.1, we demonstrate that it correctly implements the jump condition for the stresses at the liquid–vapour interface in the simulation of a layered Poiseuille flow. In § 4.2, Galilean invariance is demonstrated by measuring the dissipation of normal modes in a moving reference frame. The viscosity–capillarity coupling is probed in § 4.3 by measuring the frequency of higher-order capillary waves, in excellent agreement with Rayleigh's theory (Rayleigh 1879). We also demonstrate that the damping rate of a capillary wave agrees with the analytical solution. Validation of bulk properties is concluded by measuring the isothermal speed of sound in § 4.4, where excellent comparison to the theoretical prediction is demonstrated for large density ratios. In § 4.5, the model is extended to the simulation of a fluid–solid interface, and is validated by demonstrating the Young–Laplace law and a liquid column motion in a channel with non-uniform wettability. In § 5, the model is used to simulate water impact on textured superhydrophobic surfaces and the coalescence of mercury droplets, to demonstrate its ability to handle simulations at extremely high density ratios. Conclusions are drawn in § 6.

2. Model for two-phase flows

2.1. *Second-gradient theory: Korteweg's stress and capillary fluid equations*

In the second-gradient theory as introduced by van der Waals (1894), free energy per unit volume is expressed as

$$\mathcal{A}_{vdW} = \mathcal{A} + \tfrac{1}{2}\kappa|\nabla\rho|^2, \tag{2.1}$$

where $\mathcal{A}$ is the bulk free energy per unit volume, ρ is the density and κ is the capillary coefficient. The second term represents the interface energy while the bulk free energy is solely a function of the local density and temperature (Cahn & Hilliard 1958; Giovangigli 2020). The equilibrium state of the corresponding system is obtained by minimizing the free energy in a given volume under the constraint of constant total mass, leading to the stress tensor (Anderson *et al.* 1998),

$$\boldsymbol{T}_K = \nabla \otimes \frac{\partial \mathcal{L}}{\partial (\nabla \rho)} - \mathcal{L}\boldsymbol{I}, \tag{2.2}$$

where $\boldsymbol{I}$ is unit tensor and $\mathcal{L}$ is the Lagrange function,

$$\mathcal{L} = \mathcal{A} + \tfrac{1}{2}\kappa|\nabla\rho|^2 - \lambda\rho, \tag{2.3}$$

and λ is the Lagrange multiplier for the mass constraint, or chemical potential,

$$\lambda = \frac{\partial \mathcal{A}}{\partial \rho} - \kappa \nabla^2 \rho, \tag{2.4}$$

where ∇^2 is the Laplace operator. This in turn leads to the following Korteweg's stress tensor (Korteweg 1901):

$$\boldsymbol{T}_K = (P - \kappa \rho \nabla^2 \rho - \tfrac{1}{2}\kappa|\nabla\rho|^2)\boldsymbol{I} + \kappa \nabla\rho \otimes \nabla\rho, \tag{2.5}$$

where

$$P = \rho \frac{\partial \mathcal{A}}{\partial \rho} - \mathcal{A} \tag{2.6}$$

is the thermodynamic pressure, or equation of state. From the local balance equations for mass and momentum, one obtains the macroscopic governing laws for an isothermal capillary fluid:

$$\partial_t \rho + \nabla \cdot \rho \boldsymbol{u} = 0, \tag{2.7}$$

$$\partial_t \rho \boldsymbol{u} + \nabla \cdot \rho \boldsymbol{u} \otimes \boldsymbol{u} + \nabla \cdot \boldsymbol{T} = 0, \tag{2.8}$$

where $\boldsymbol{u}$ is the fluid velocity and the stress tensor $\boldsymbol{T}$ is

$$\boldsymbol{T} = \boldsymbol{T}_K + \boldsymbol{T}_{NS}. \tag{2.9}$$

The Navier–Stokes viscous stress tensor reads

$$\boldsymbol{T}_{NS} = -\mu\boldsymbol{S} - \eta(\nabla \cdot \boldsymbol{u})\boldsymbol{I}, \tag{2.10}$$

where $\boldsymbol{S}$ is the trace-free rate-of-strain tensor,

$$\boldsymbol{S} = \nabla\boldsymbol{u} + \nabla\boldsymbol{u}^\dagger - \tfrac{2}{3}(\nabla \cdot \boldsymbol{u})\boldsymbol{I}, \tag{2.11}$$

and μ and η are the dynamic and the bulk viscosity, respectively.

The momentum balance equation in (2.8) can be recast in the following form:

$$\partial_t \rho \boldsymbol{u} + \nabla \cdot \rho \boldsymbol{u} \otimes \boldsymbol{u} + \boldsymbol{F}_K + \nabla \cdot \boldsymbol{T}_{NS} = 0, \tag{2.12}$$

where Korteweg's *force* $\boldsymbol{F}_K$ is the divergence of the Korteweg pressure tensor,

$$\boldsymbol{F}_K = \nabla \cdot \boldsymbol{T}_K. \tag{2.13}$$

The latter can be written in the following form:

$$\boldsymbol{F}_K = \nabla P_0 + \nabla(P - P_0) - \kappa\rho\nabla(\nabla^2\rho), \tag{2.14}$$

where we have introduced a *reference pressure* P_0. Navier–Stokes momentum equations with Korteweg's force in (2.14) shall be a target for reconstruction by a suitable kinetic model.

2.2. *Kinetic model for non-ideal fluid*

To introduce a kinetic model for non-ideal fluid, we begin with the first Bogolioubov–Born–Green–Kirkwood–Yvon (BBGKY) equation,

$$\partial_t f + \boldsymbol{v} \cdot \nabla f = \mathcal{J} = \iint \nabla V(|\boldsymbol{r} - \boldsymbol{r}_1|) \cdot \frac{\partial}{\partial \boldsymbol{v}} f_2(\boldsymbol{r}, \boldsymbol{v}, \boldsymbol{r}_1, \boldsymbol{v}_1, t) \, \mathrm{d}\boldsymbol{v}_1 \, \mathrm{d}\boldsymbol{r}_1, \tag{2.15}$$

where $f(\boldsymbol{r}, \boldsymbol{v}, t)$ and $f_2(\boldsymbol{r}, \boldsymbol{v}, \boldsymbol{r}_1, \boldsymbol{v}_1, t)$ are the one- and the two-particle distribution functions, respectively, $\boldsymbol{r}$, $\boldsymbol{r}_1$ and $\boldsymbol{v}$, $\boldsymbol{v}_1$ are particles' position and velocity, while V is a potential of a pair interaction. The local equilibrium state is defined by the Maxwellian f^{eq} at constant temperature T, parametrized by the local values of density ρ and flow velocity $\boldsymbol{u}$,

$$f^{eq} = \frac{\rho}{(2\pi RT)^{3/2}} \exp\left[-\frac{(\boldsymbol{v} - \boldsymbol{u})^2}{2RT} \right], \tag{2.16}$$

where R is the gas constant. Furthermore, let us introduce a projector $\mathcal{K}$ onto local equilibrium at constant temperature (Gorban & Karlin 2005),

$$\mathcal{K}\mathcal{J} = \left(\frac{\partial f^{eq}}{\partial \rho} - \frac{1}{\rho}\boldsymbol{u} \cdot \frac{\partial f^{eq}}{\partial \boldsymbol{u}} \right) \int \mathcal{J} \, \mathrm{d}\boldsymbol{v} + \frac{1}{\rho} \frac{\partial f^{eq}}{\partial \boldsymbol{u}} \cdot \int \boldsymbol{v} \mathcal{J} \, \mathrm{d}\boldsymbol{v}. \tag{2.17}$$

The projector property, $\mathcal{K}^2 = \mathcal{K}$, can be verified by a direct computation. With the projector in (2.17), the interaction term in (2.15) is split into two parts by writing an identity,

$$\mathcal{J} = (1 - \mathcal{K})\mathcal{J} + \mathcal{K}\mathcal{J}. \tag{2.18}$$

The first term,

$$\mathcal{J}_{loc} = (1 - \mathcal{K})\mathcal{J}, \tag{2.19}$$

satisfies the local conservation of both mass and momentum,

$$\mathcal{K}\mathcal{J}_{loc} = 0. \tag{2.20}$$

It is conventional to model the locally conserving part of the interaction with a single relaxation time Bhatnagar–Gross–Krook (BGK) approximation,

$$\mathcal{J}_{loc} \rightarrow \mathcal{J}_{BGK} = -\frac{1}{\tau}(1 - \mathcal{K})f = -\frac{1}{\tau}(f - f^{eq}), \tag{2.21}$$

where the relaxation time τ is a free parameter. The second term in the identity of (2.18),

$$\mathcal{J}_{nloc} = \mathcal{K}\mathcal{J}, \tag{2.22}$$

satisfies the local mass but not the local momentum conservation. Indeed, after integration by part in the velocity $\boldsymbol{v}$ and neglecting boundary integrals, we arrive at

$$\mathcal{J}_{nloc} = -\frac{1}{\rho} \frac{\partial f^{eq}}{\partial \boldsymbol{u}} \cdot \boldsymbol{F}_{nloc}, \tag{2.23}$$

where the force $\boldsymbol{F}_{nloc}$ reads

$$\boldsymbol{F}_{nloc} = \iiint \nabla V(|\boldsymbol{r} - \boldsymbol{r}_1|) f_2(\boldsymbol{r}, \boldsymbol{v}, \boldsymbol{r}_1, \boldsymbol{v}_1, t) \, \mathrm{d}\boldsymbol{v}_1 \, \mathrm{d}\boldsymbol{r}_1 \, \mathrm{d}\boldsymbol{v}. \tag{2.24}$$

Collecting the BGK approximation together with the non-local contribution, a generic kinetic model may be written as

$$\partial_t f + \boldsymbol{v} \cdot \boldsymbol{\nabla} f = -\frac{1}{\tau}(f - f^{eq}) - \frac{1}{\rho}\frac{\partial f^{eq}}{\partial \boldsymbol{u}} \cdot \boldsymbol{F}_{nloc}. \tag{2.25}$$

Evaluation of the force in (2.24) requires us to specify the particles interaction. It is customary to invoke the Enskog–Vlasov model (Enskog 1921; Vlasov 1961), where both hard-sphere collisions and a weak long-range attraction potential contribute to a non-local momentum transfer. For the hard-sphere Enskog part, a de-localization of the collision is responsible for a non-vanishing contribution of momentum transfer through the distance between the centres of the spheres upon their impact while the Vlasov approximation contributes non-locally to the momentum transfer from a distributed mean-field force. Evaluation of both the Enskog and Vlasov contributions to the force in (2.24) proceeds along familiar lines (Chapman & Cowling 1939; He *et al.* 1998; He & Doolen 2002; Martys 2006) and is reported in Appendices A and B for completeness,

$$\boldsymbol{F}_{EV} = \boldsymbol{F}_E + \boldsymbol{F}_V. \tag{2.26}$$

The first term is the lowest-order contribution of the collisional momentum transfer from the Enskog hard-sphere model,

$$\boldsymbol{F}_E = \boldsymbol{\nabla} b\rho^2 \chi RT + O(\nabla^3 \rho). \tag{2.27}$$

Here $b = 4v_{HS}$, with $v_{HS} = \mathcal{V}_{HS}/m$ the specific volume of a hard sphere of diameter d and mass m, while $\mathcal{V}_{HS} = \pi d^3/6$ is the volume of the sphere. Moreover, χ is the equilibrium two-particle correlation function, evaluated at the local density reduced by the specific volume of the hard sphere, $\chi = \chi(b\rho(\boldsymbol{r}, t))$. To the lowest order, $\chi = 1 + (5/8)b\rho + O((b\rho)^2)$, cf. Chapman & Cowling (1939). The second term in (2.26) is the contribution of a long-range attraction potential V in the mean field Vlasov approximation. To third order in the gradient of density,

$$\boldsymbol{F}_V = -\boldsymbol{\nabla} a\rho^2 - \kappa\rho\boldsymbol{\nabla}\nabla^2\rho + O(\nabla^5 \rho), \tag{2.28}$$

where parameters a and κ are

$$a = -2\pi \int_d^\infty r^2 V(r)\,\mathrm{d}r, \tag{2.29}$$

$$\kappa = -\frac{2\pi}{3} \int_d^\infty r^4 V(r)\,\mathrm{d}r. \tag{2.30}$$

Thus, with the approximations specified, the non-local force in (2.26) becomes

$$\boldsymbol{F}_{EV} = \boldsymbol{\nabla}(P_{EV} - P_0) - \kappa\rho\boldsymbol{\nabla}\nabla^2\rho, \tag{2.31}$$

where the reference ideal gas pressure P_0 is provided by the local Maxwellian in (2.16),

$$P_0 = \frac{1}{3} \int |\boldsymbol{v} - \boldsymbol{u}|^2 f^{eq}\,\mathrm{d}\boldsymbol{v} = \rho RT, \tag{2.32}$$

while the equation of state of the Enskog–Vlasov gas is of van der Waals type,

$$P_{EV} = \rho RT(1 + b\rho\chi) - a\rho^2. \tag{2.33}$$

This allows us to extend the Enskog–Vlasov kinetic model, and a phenomenological equation of state P in (2.6) can be used instead of P_{EV} in (2.33). Moreover, the reference

pressure P_0 can be made selective by rescaling the local equilibrium,

$$f^{eq} = \frac{\rho}{(2\pi P_0/\rho)^{D/2}} \exp\left[-\frac{(\boldsymbol{v} - \boldsymbol{u})^2}{2P_0/\rho}\right], \tag{2.34}$$

where D is the space dimension. While the Enskog–Vlasov partition above corresponds to selecting $P_0 = \rho RT$, an alternative is provided by Reyhanian, Dorschner & Karlin (2020), where $P_0 = P$ is chosen. Another construction was proposed (Martys 1999, 2001) where all contributions to the pressure tensor are introduced with the local attractor, rescaling temperature and introducing a velocity shift to match the targeted system of moments. Using the rescaled equilibria in (2.34), a family of kinetic models parametrized by the reference pressure reads

$$\partial_t f + \boldsymbol{v} \cdot \nabla f = -\frac{1}{\tau}(f - f^{eq}) - \frac{1}{\rho}\frac{\partial f^{eq}}{\partial \boldsymbol{u}} \cdot [\nabla(P - P_0) - \kappa\rho\nabla\nabla^2\rho]. \tag{2.35}$$

The kinetic equation in (2.35) shall be considered as a semi-phenomenological model of a non-ideal fluid, with the relaxation time τ, the capillarity coefficient κ, pressure P and reference pressure P_0 as phenomenological input parameters, while the Enskog–Vlasov realization will serve as a representative example for estimates of various flow regimes.

The analysis of the kinetic model in (2.35) under the conventional scaling of a small deviation from a uniform state (Chapman & Cowling 1939),

$$\nabla \to \epsilon\nabla, \quad \partial_t \to \epsilon\partial_t, \tag{2.36a,b}$$

is detailed in Appendix C. To second order in space derivatives, the resulting momentum balance equation reads

$$\partial_t\rho\boldsymbol{u} + \epsilon\nabla \cdot \rho\boldsymbol{u} \otimes \boldsymbol{u} + \epsilon\nabla P + \epsilon\nabla \cdot \epsilon\boldsymbol{T}_{NS} + O(\epsilon^3) = 0, \tag{2.37}$$

where the dynamic viscosity μ and the bulk viscosity η in the Navier–Stokes stress tensor in (2.10) are defined by the reference pressure ($D = 3$),

$$\mu = \tau P_0, \tag{2.38}$$

$$\eta = \left(\frac{5}{3} - \frac{\partial \ln P_0}{\partial \ln \rho}\right)\tau P_0. \tag{2.39}$$

Thus, the momentum balance equation in (2.37) is form-invariant with respect to the choice of reference pressure, provided P_0 satisfies a sub-isentropic condition,

$$P_0 \leq C\rho^{5/3}, \tag{2.40}$$

for some $C > 0$. With (2.40), the bulk viscosity in (2.39) is positive and vanishes when the reference pressure follows an isentropic process for ideal monatomic gas, $P_0 = C\rho^{5/3}$. For example, any polytropic process, $P_0 = A\rho^n$, $1 \leq n \leq 5/3$ satisfies the sub-isentropic condition and results in $\eta = (5/3 - n)\tau P_0$. A special case of the isothermal process $n = 1$ returns $\eta = (2/3)\tau P_0$, and the viscous stress tensor becomes

$$\boldsymbol{T}_{NS} = -\tau P_0(\nabla\boldsymbol{u} + \nabla\boldsymbol{u}^\dagger). \tag{2.41}$$

However, when compared to the two-phase momentum equation in (2.12), the macroscopic limit recovers only the non-ideal gas component thereof while missing Korteweg's

capillarity contribution. Indeed, the third-order term, $\sim \epsilon^3 \rho \nabla \nabla^2 \rho$ in (2.28) and (2.35), does *not* contribute to the momentum equation in (2.37) under the scaling of (2.36*a,b*). This is consistent with the well-known results from kinetic theory (Chapman & Cowling 1939) and is not surprising. The scaling of (2.36*a,b*) is essentially based on the Knudsen number, which overrides the relative contribution of the capillarity term by two orders, cf. Appendix C. Thus, under the weak non-uniformity assumption in (2.36*a,b*), the capillarity terms are seen as higher-order Burnett-level contributions, and cannot appear in the main (first and second) orders in the momentum balance equation of (2.37). In fact, the condition in (2.36*a,b*) rules out situations at an interface between phases where gradients of density become large over a relatively short distance. Therefore, for the kinetic model in (2.35) to recover in-full the momentum balance in (2.12), a different scaling needs to be applied.

2.3. *Scaling by velocity increment and lattice Boltzmann equation*

2.3.1. *Time step and forcing*

A rescaling of the kinetic model in this section shall be maintained by introducing a time step δt. As a preliminary consideration, we evaluate the contribution of the force term over the time step. To that end, as noted by Kupershtokh, Medvedev & Karpov (2009), for a generic force $\boldsymbol{F}$, we can write the action of the force on the distribution function as a full derivative in a frame that moves with the local fluid velocity,

$$\frac{1}{\rho} \frac{\partial f^{eq}}{\partial \boldsymbol{u}} \cdot \boldsymbol{F} = \frac{\mathrm{d} f^{eq}}{\mathrm{d} t}. \tag{2.42}$$

Introducing the *velocity increment*,

$$\delta \boldsymbol{u} = \frac{\boldsymbol{F}}{\rho} \delta t, \tag{2.43}$$

and integrating in time, leads to an approximation,

$$\mathcal{F} = \int_t^{t+\delta t} \frac{1}{\rho} \frac{\partial f^{eq}}{\partial \boldsymbol{u}} \cdot \boldsymbol{F} \, \mathrm{d}t \approx f^{eq}(\boldsymbol{u} + \delta \boldsymbol{u}) - f^{eq}(\boldsymbol{u}). \tag{2.44}$$

This so-called exact difference method (EDM) becomes accurate for a gravity force, $\boldsymbol{F}/\rho = \text{const.}$, otherwise it often provides a reliable estimate for the force term and is widely used. In what follows, the scaling to be applied assumes smallness of the velocity increment in (2.43) rather than smoothness of the spatial distribution of the force. Since the velocity increment is based on a time step, it is natural to proceed with a lattice Boltzmann realization of the kinetic equation.

2.3.2. *Standard lattice and product form*

The lattice Boltzmann model shall be realized with the standard discrete velocity set $D3Q27$, where $D = 3$ stands for three dimensions and $Q = 27$ is the number of discrete

953 A4-8

velocities,

$$c_i = (c_{ix}, c_{iy}, c_{iz}), \quad c_{i\alpha} \in \{-1, 0, 1\}. \tag{2.45a,b}$$

We first define a triplet of functions in two variables, ξ_α and $\zeta_{\alpha\alpha}$,

$$\Psi_0(\xi_\alpha, \zeta_{\alpha\alpha}) = 1 - \zeta_{\alpha\alpha}, \tag{2.46}$$

$$\Psi_1(\xi_\alpha, \zeta_{\alpha\alpha}) = \frac{\xi_\alpha + \zeta_{\alpha\alpha}}{2}, \tag{2.47}$$

$$\Psi_{-1}(\xi_\alpha, \zeta_{\alpha\alpha}) = \frac{-\xi_\alpha + \zeta_{\alpha\alpha}}{2}, \tag{2.48}$$

and consider a product form associated with the discrete velocities c_i in (2.45a,b),

$$\Psi_i = \Psi_{c_{ix}}(\xi_x, \zeta_{xx}) \Psi_{c_{iy}}(\xi_y, \zeta_{yy}) \Psi_{c_{iz}}(\xi_z, \zeta_{zz}). \tag{2.49}$$

All pertinent populations below shall be determined by specifying the parameters ξ_α and $\zeta_{\alpha\alpha}$ in the product form in (2.49). A two-dimensional version of the model on the *D2Q9* lattice is obtained by omitting the *z*-component in all formulae below. Finally, we use the notation $\delta r_i = c_i \delta t$ for the *lattice links*, and denote the *grid spacing* in any direction $\alpha = x, y, z$ as $\delta r = |c_{i\alpha}| \delta t, c_{i\alpha} \neq 0$. For the *D3Q27* discrete velocity set in (2.45a,b), the lattice spacing is the same in all Cartesian directions.

2.3.3. *The lattice Boltzmann equation*

The local density ρ and flow velocity u are defined using the populations f_i,

$$\rho(r, t) = \sum_{i=0}^{Q-1} f_i(r, t), \tag{2.50}$$

$$\rho u(r, t) = \sum_{i=0}^{Q-1} c_i f_i(r, t). \tag{2.51}$$

With a reference pressure P_0, and by setting the parameters,

$$\xi_\alpha = u_\alpha, \tag{2.52}$$

$$\zeta_{\alpha\alpha} = \frac{P_0}{\rho} + u_\alpha^2, \tag{2.53}$$

the local equilibrium populations are represented with the product-form in (2.49),

$$f_i^{eq} = \rho \prod_{\alpha=x,y,z} \Psi_{c_{i\alpha}} \left(u_\alpha, \frac{P_0}{\rho} + u_\alpha^2 \right). \tag{2.54}$$

The LBGK equation, supplemented with a forcing term, is written as

$$f_i(r + c_i \delta t, t + \delta t) - f_i(r, t) = \omega(f_i^{eq} - f_i) + (f_i^* - f_i^{eq}), \tag{2.55}$$

where ω is a dimensionless relaxation parameter, the equilibrium populations are provided by (2.54), while the extended equilibrium populations f_i^* are defined by the product-form

in (2.49) with the following assignment for the parameters:

$$\xi_\alpha^* = u_\alpha + \frac{F_\alpha \delta t}{\rho}, \tag{2.56}$$

$$\zeta_{\alpha\alpha}^* = \frac{P_0}{\rho} + u_\alpha^2 + \frac{\Phi_{\alpha\alpha}}{\rho}, \tag{2.57}$$

where $\Phi_{\alpha\alpha}/\rho$ is a correction term for the diagonals of the non-equilibrium momentum flux tensor,

$$\Phi_{\alpha\alpha} = \left(1 - \frac{\omega}{2}\right) \delta t \partial_\alpha \left(\rho u_\alpha \left(u_\alpha^2 + \frac{3P_0}{\rho} - 3\varsigma^2\right)\right), \tag{2.58}$$

where $\varsigma = \delta r/\sqrt{3}\delta t$ is the so-called lattice speed of sound. The form of the correction term is a result of the multi-scale analysis presented in Appendix D. Thus, the extended equilibrium is explicitly written as

$$f_i^* = \rho \prod_{\alpha=x,y,z} \Psi_{c_{i\alpha}} \left(u_\alpha + \frac{F_\alpha \delta t}{\rho}, \frac{P_0}{\rho} + u_\alpha^2 + \frac{\Phi_{\alpha\alpha}}{\rho}\right). \tag{2.59}$$

Comments are in order.

- If the correction term of (2.58) is omitted in (2.57), the population in (2.59) becomes the equilibrium with the increment δu in (2.43) due to force action added to the flow velocity u. This corresponds to the EDM forcing maintained by the second bracket in the right-hand side of the LBGK equation in (2.55).
- The correction term in (2.56) is added following a proposal by Saadat *et al.* (2021). Its purpose is to compensate for the bias of the $D3Q27$ velocities in (2.45*a,b*), $c_{i\alpha}^3 = c_{i\alpha}$, and to restore the Galilean invariance of the normal components of the viscous stress tensor.

The LBGK model in (2.55) is generic with respect to the choice of reference pressure P_0 and the force F. We now proceed with the special case of Korteweg's force to establish a representation thereof matched to the lattice Boltzmann system.

2.3.4. *Pseudo-potential and capillarity*

Following the representation in (2.14), Korteweg's force includes two distinct parts, the term supplying the non-ideal gas equation of state and the capillarity term responsible for the surface tension. Introducing a pseudo-potential ψ,

$$\psi = \begin{cases} \sqrt{P - P_0} & \text{if } P > P_0, \\ \sqrt{P_0 - P} & \text{if } P \leq P_0, \end{cases} \tag{2.60}$$

Korteweg's force is written as

$$F = \begin{cases} 2\psi\nabla\psi - \kappa\rho\nabla\nabla^2\rho & \text{if } P > P_0, \\ -2\psi\nabla\psi - \kappa\rho\nabla\nabla^2\rho & \text{if } P \leq P_0. \end{cases} \tag{2.61}$$

In the lattice Boltzmann setting, the pseudo-potential part is represented as a linear combination of the first- and second-neighbours contributions,

$$\delta t \psi(\mathbf{r})\nabla\psi(\mathbf{r}) = \psi(\mathbf{r}) \sum_{i=0}^{Q-1} \frac{w_i}{\varsigma^2} c_i [\mathcal{G}_1 \psi(\mathbf{r} + c_i\delta t) + \mathcal{G}_2 \psi(\mathbf{r} + 2c_i\delta t)] + O([\delta r \nabla]^5), \tag{2.62}$$

953 A4-10

where the weights w_i are defined by the product-form in (2.49) at $\xi_\alpha = 0$, $\zeta_{\alpha\alpha} = \varsigma^2$,

$$w_i = \prod_{\alpha=x,y,z} \Psi_{c_{i\alpha}}(0, \varsigma^2), \tag{2.63}$$

and where the parameters $\mathcal{G}_1$ and $\mathcal{G}_2$ satisfy the conditions,

$$\mathcal{G}_1 + 2\mathcal{G}_2 = 1, \tag{2.64}$$

$$\mathcal{G}_1 + 8\mathcal{G}_2 = 0. \tag{2.65}$$

The condition in (2.64) maintains the equation of state, while the condition in (2.65) eliminates the third-order error. Non-compliance with the first and/or second condition would introduce respectively deviations of order $O([\delta r \nabla])$ and/or $O([\delta r \nabla]^3)$ from the target Korteweg stress tensor.

The capillarity part of Korteweg's force in (2.61) is represented in a similar way but using the density instead of the pseudo-potential,

$$\delta t \tilde{\kappa} \rho(\mathbf{r}) \nabla \nabla^2 \rho(\mathbf{r}) = \rho(\mathbf{r}) \sum_{i=0}^{Q-1} \frac{w_i}{\varsigma^2} \mathbf{c}_i [\mathcal{G}_3 \rho(\mathbf{r} + \mathbf{c}_i \delta t) + \mathcal{G}_4 \rho(\mathbf{r} + 2\mathbf{c}_i \delta t)]$$
$$+ O([\delta r \nabla]^5), \tag{2.66}$$

where $\tilde{\kappa} = \kappa \delta r^2$ and the parameters $\mathcal{G}_3$ and $\mathcal{G}_4$ satisfy the conditions,

$$\mathcal{G}_3 + 2\mathcal{G}_4 = 0, \tag{2.67}$$

$$\mathcal{G}_3 + 8\mathcal{G}_4 = 6\kappa. \tag{2.68}$$

The condition in (2.67) cancels the first-order derivative, while the condition in (2.68) maintains the capillarity contribution. Combining both contributions of the pseudo-potential in (2.62) and the capillarity in (2.66), we obtain the lattice Boltzmann form of Korteweg's force in (2.61) as

$$\delta t \mathbf{F} = \pm 2 \psi(\mathbf{r}) \sum_{i=0}^{Q-1} \frac{w_i}{\varsigma^2} \mathbf{c}_i \left[\frac{4}{3} \psi(\mathbf{r} + \mathbf{c}_i \delta t) - \frac{1}{6} \psi(\mathbf{r} + 2\mathbf{c}_i \delta t) \right]$$
$$+ \tilde{\kappa} \rho(\mathbf{r}) \sum_{i=0}^{Q-1} \frac{w_i}{\varsigma^2} \mathbf{c}_i [2\rho(\mathbf{r} + \mathbf{c}_i \delta t) - \rho(\mathbf{r} + 2\mathbf{c}_i \delta t)] + O([\delta r \nabla]^5), \tag{2.69}$$

where the sign convention follows (2.61).

In the context of the lattice Boltzmann method, various pseudo-potential representations have long been in use, and comments are to make a distinction to the present formulation.

- By setting $\mathcal{G}_2 = 0$ in (2.62) and ignoring Korteweg's capillarity term in (2.66) by choosing $\mathcal{G}_3 = \mathcal{G}_4 = 0$, one recovers a model first proposed by Shan & Chen (1993) for special equations of state (see (G1), (G2), (G3) in Appendix G) and extended to a general equation of state by Yuan & Schaefer (2006). Unlike the above condition in (2.65) which eliminates the third-order error in the pseudo-potential part of Korteweg's force in (2.14), the model of Shan & Chen (1993) requires the third-order Korteweg-like term to be retained so that it mimics surface

tension effects. Consequently, the force in the models of Shan & Chen (1993), Yuan & Schaefer (2006) becomes

$$\boldsymbol{F}_{SC} = 2\psi\boldsymbol{\nabla}\psi + \tfrac{1}{3}\psi\boldsymbol{\nabla}\boldsymbol{\nabla}^2\psi. \qquad (2.70)$$

The force in (2.70) neither conforms with the van der Waals second-gradient theory and Korteweg's stress of §2.1 (unless $\psi = A\rho$ which, however, does not lead to phase separation), nor can it be derived from the BBGKY equation with a central-force particles interaction of §2.2. Another relatively minor issue is the fixed parameter 1/3, which is mimicking the capillarity coefficient and is the result of the third-order error retained in the expansion.

- By imposing the condition in (2.64) while still discarding Korteweg's capillarity contribution in (2.66), one arrives at a dual-range force model of Sbragaglia *et al.* (2007), Shan (2008),

$$\boldsymbol{F}_{DR} = 2\psi\boldsymbol{\nabla}\psi + (\tfrac{4}{3} - \mathcal{G}_1)\psi\boldsymbol{\nabla}\boldsymbol{\nabla}^2\psi. \qquad (2.71)$$

The model in (2.71) is an improvement on the first-neighbour model in (2.70), in that it allows for a variable capillarity-like coefficient. At the same time, it does not resolve the inconsistency with Korteweg's stress tensor.

- Various other modifications of the original models of Shan & Chen (1993) were proposed to improve on the main inconsistency by introducing and tuning *ad hoc* numerical coefficients tailored to a selected equation of state (Kupershtokh *et al.* 2009; Li, Luo & Li 2013; Huang, Yin & Killough 2019; Luo, Fei & Wang 2021). However, to the best of our knowledge, none of these proposals came to recognize that the problem lies in the fact that it is impossible to represent both parts of Korteweg's force, the non-ideal equation of state and the capillarity term, while using a pseudo-potential alone. This fact follows both from the phenomenological thermodynamics reviewed in §2.1, as well as from a more microscopic approach of §2.2. The pseudo-potential in both cases represents only the equation of state, while the capillarity term requires the density field to be used, as featured by (2.66).

- Pseudo-potential is a convenient form of representing the equation of state contribution to Korteweg's force, tailored to the lattice Boltzmann setting. If other numerical methods are used to evaluate the force in (2.61), such as higher-order finite difference, the model is usually renamed to a free energy approach.

With the generic LBGK model in (2.55) and Korteweg's force in (2.69) both specified, we proceed to the analysis of the hydrodynamic limit under a suitable scaling.

2.3.5. *Hydrodynamic limit under small velocity increment scaling*

Chapman–Enskog analysis of the LBGK equation in (2.55) was performed under the following scaling. With the characteristic values of the flow velocity $\mathcal{U}$, the flow scale $\mathcal{L}$, the density ρ, the force $\mathcal{F}$ and the velocity increment δu, the following conditions apply:

$$\frac{\delta u}{\mathcal{U}} \sim \frac{\delta t \mathcal{F}}{\rho \mathcal{U}} \sim \varepsilon, \qquad (2.72)$$

$$\frac{\delta r}{\mathcal{L}} \sim \varepsilon. \qquad (2.73)$$

The first scaling condition in (2.72) refers to a *smallness of velocity increment*, that is, to the smallness of the force action over time δt. The second scaling condition in (2.73) is

a *resolution requirement*. Both conditions are assumed to hold simultaneously. Details of the analysis are provided in Appendix D while the result is summarized below.

Let us introduce a transformed velocity U by shifting the local velocity u by half of the velocity increment δu in (2.43),

$$U = u + \varepsilon \frac{\delta t F}{2\rho}. \tag{2.74}$$

Then the following mass and momentum balance equations to second order in ε are recovered when the force in (2.69) is used under the scaling in (2.72) and (2.73),

$$\partial_t \rho + \varepsilon \nabla \cdot \rho U + O(\varepsilon^3) = 0, \tag{2.75}$$

$$\partial_t \rho U + \varepsilon \nabla \cdot \rho U \otimes U + \varepsilon F_K + \varepsilon \nabla \cdot \varepsilon T_{NS} + O(\varepsilon^3) = 0, \tag{2.76}$$

where the dynamic and the bulk viscosity in the Navier–Stokes stress tensor in (2.10) are related to the relaxation parameter ω and the reference pressure P_0 as follows:

$$\mu = \left(\frac{1}{\omega} - \frac{1}{2} \right) \delta t P_0, \tag{2.77}$$

$$\eta = \left(\frac{5}{3} - \frac{\partial \ln P_0}{\partial \ln \rho} \right) \left(\frac{1}{\omega} - \frac{1}{2} \right) \delta t P_0. \tag{2.78}$$

Unlike the previous result in (2.37), the momentum balance in (2.76) includes not only the non-ideal gas pressure but also the capillarity term, and is thus consistent with Korteweg's force in the momentum balance. It should be pointed out that the scaling in (2.72) refers to the smallness of the increment of the flow velocity rather than to the smallness of either the time step or of the force. Thus, rescaling the kinetic model in (2.35) based on the smallness of the flow velocity increments results in both the non-ideal gas equation of state and the capillarity revealed at the Euler level $O(\varepsilon)$ of the momentum balance in (2.76). This is in contrast to the conventional scaling, which is tied to the non-uniformity and surface tension that would appear only at a Burnett level $O(\epsilon^3)$.

2.3.6. *Code structure*

The structure of the algorithm is given in figure 1. The algorithm consists of four main building blocks: (a) evaluation of macroscopic variables ρ, u and P_0 via (2.50); (b) evaluation of non-local macroscopic contributions $\Phi_{\alpha\alpha}$ and F_α via (2.58), (2.69) and (2.60); (c) evaluation of equilibrium and extended equilibrium functions via (2.54) and (2.59) and (d) discrete space/time evolution following (2.55).

In the remainder of this paper, and without loss of generality, we set the reference pressure $P_0 = \varsigma^2 \rho$ to minimize the correction term in (2.58). This choice of reference pressure follows the third-order quadrature leading to the family of lattices used here and is quite common in both ideal and non-ideal fluid lattice Boltzmann simulations (Krüger *et al.* 2017). Other possibilities of choosing the reference pressure are illustrated in Appendix H. In the next section, the model is scrutinized by a set of numerical tests probing various aspects of thermo- and hydrodynamic consistency.
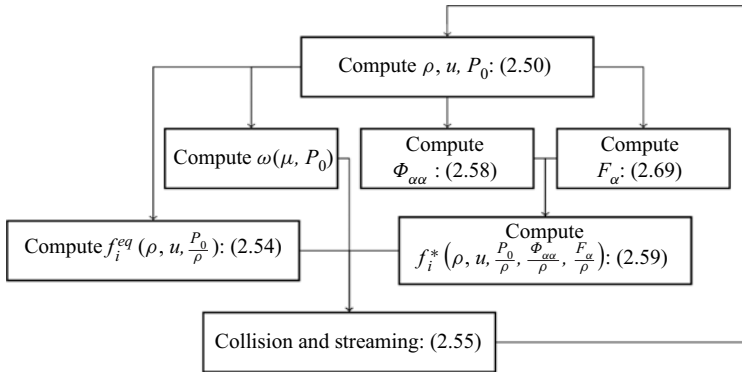
Figure 1. Flow chart for a typical code based on the proposed two-phase lattice Boltzmann model.

3. Thermodynamic consistency

3.1. *Liquid–vapour coexistence*

We begin with the validation of liquid–vapour coexistence. Two-dimensional flat interface simulations were performed on a grid 800×10, filled with the vapour phase of a fluid with a specified equation of state and periodic boundary conditions. A column of the liquid phase over 400 grid-points was placed at the centre of the domain. Simulations were ran until the steady state was reached. The steady state was monitored via an L_0 norm convergence criterion based on the liquid density ρ_l at the centre of the drop and the vapour density ρ_v at a location outside the drop. A theoretical prediction for the coexistence density ratio ρ_l/ρ_v is readily obtained via the equilibrium condition leading to the Maxwell equal-area construction,

$$\int_{\rho_v}^{\rho_l} \frac{P_{sat} - P}{\rho^2}\, \mathrm{d}\rho = 0, \tag{3.1}$$

where $P_{sat}(T)$ is the saturation pressure at which the liquid and vapour phases coexist at a given temperature T below the critical point.

Initially, four generally adopted equations of state (EoS) were considered: the van der Waals EoS (van der Waals 1873),

$$P = \frac{\rho RT}{1 - b\rho} - a\rho^2, \tag{3.2}$$

where parameters a and b are related to critical temperature T_c and pressure P_c as

$$a = \frac{27}{64} \frac{R^2 T_c^2}{P_c}, \quad b = \frac{1}{8} \frac{RT_c}{P_c}; \tag{3.3a,b}$$

the Peng–Robinson EoS (Peng & Robinson 1976),

$$P = \frac{\rho RT}{1 - b\rho} - \frac{a\alpha(T)\rho^2}{1 + 2\rho b - b^2\rho^2}, \tag{3.4}$$

with

$$\alpha(T) = [1 + (0.37464 + 1.54226\omega' - 0.26992\omega'^2)(1 - \sqrt{T/T_c})]^2, \tag{3.5}$$

953 A4-14

where ω' the acentric factor ($\omega' = 0.344$ for water), and

$$a = 0.45724\frac{R^2 T_c^2}{P_c}, \quad b = 0.0778\frac{RT_c}{P_c}; \tag{3.6a,b}$$

the Riedlich–Kwong–Soave EoS (Redlich & Kwong 1949; Soave 1972),

$$P = \frac{\rho RT}{1 - b\rho} - \frac{a\alpha(T)\rho^2}{1 + \rho b}, \tag{3.7}$$

with

$$\alpha(T) = [1 + (0.480 + 1.574\omega' - 0.176\omega'^2)(1 - \sqrt{T/T_c})]^2, \tag{3.8}$$

and

$$a = 0.42748\frac{R^2 T_c^2}{P_c}, \quad b = 0.08664\frac{RT_c}{P_c}; \tag{3.9a,b}$$

and the Carnahan–Starling EoS (Carnahan & Starling 1969),

$$P = \rho RT\frac{1 + b\rho/4 + (b\rho/4)^2 - (b\rho/4)^3}{(1 - b\rho/4)^3} - a\rho^2, \tag{3.10}$$

with

$$a = 0.4963\frac{R^2 T_c^2}{P_c}, \quad b = 0.18727\frac{RT_c}{P_c}. \tag{3.11a,b}$$

Figure 2 demonstrates that the stationary density ratios ρ_l/ρ_v obtained from the simulation are in excellent agreement with the theoretical coexisting liquid–vapour density ratios that are defined by Maxwell's equal-area rule in (3.1), for all four equations of state and for ratios as high as at least $\rho_l/\rho_v \sim 10^{11}$. It is noted that high coexisting density ratios were obtained without any tuning parameters, universally for all equations of state considered. Therefore, and without loss of generality, in the remainder of this article, we only consider the van der Waals equation of state in (3.2).

3.2. *The principle of corresponding states and thermodynamic convergence*

A discussion on the principle of corresponding states and the necessity of adherence to it in the context of the van der Waals theory of a capillary fluid in the simulation of realistic systems at large density ratios is in order. According to Guggenheim (1945), the principle of corresponding states is 'the most useful byproduct of van der Waals' equation of state'. The principle maintains that all properties that depend on inter-molecular forces are related to the critical properties of the substance in a universal way, regardless of the molecular compound of interest. While for real fluids, as shown by Guggenheim (1945), the principle is an approximation, it is an exact property within the van der Waals capillary fluids theory. This is, most notably, shown by the absence of substance-dependent parameters in the non-dimensional form of the van der Waals equation of state and mean-field scaling laws. For the equation of state, the principle of corresponding states implies that the reduced pressure $P_r = P/P_c$ is a universal function of the reduced temperature $T_r = T/T_c$ and of
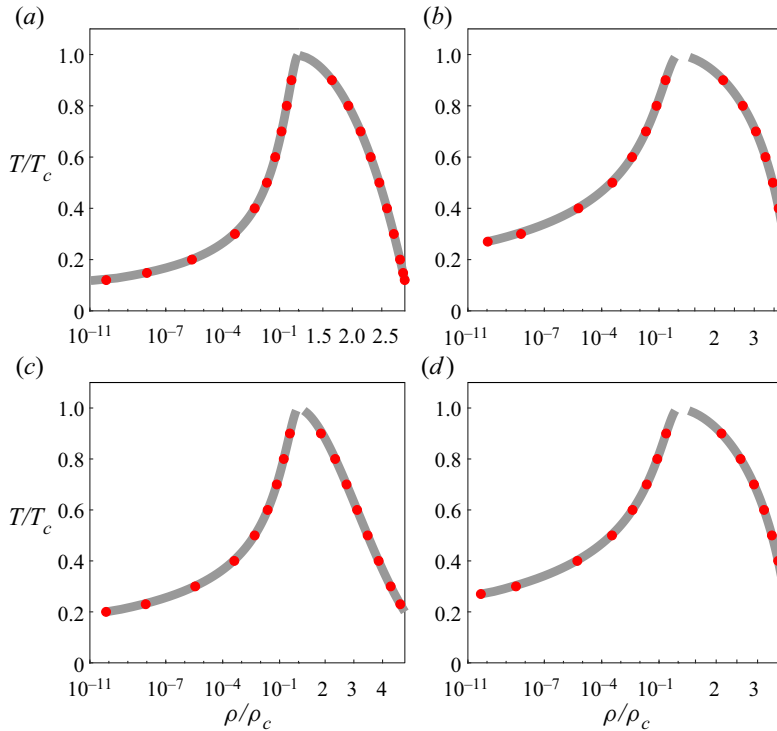
Figure 2. Liquid–vapour coexistence for various equations of state. Grey lines, Maxwell's equal-area construction in (3.1). Red symbol, simulation. (*a*) van der Waals (3.2) (*a* = 0.000159, *b* = 0.0952); (*b*) Peng–Robinson (3.4) (*a* = 0.000159, *b* = 0.0952); (*c*) Carnahan–Starling (3.10) (*a* = 0.000868, *b* = 4); (*d*) Riedlich–Kwong–Soave (3.7) (*a* = 0.000159, *b* = 0.0952). For all simulations, $\tilde{\kappa} = 0.02$.

the reduced density $\rho_r = \rho/\rho_c$,

$$\frac{P}{P_c} = f\left(\frac{T}{T_c}, \frac{\rho}{\rho_c}\right). \tag{3.12}$$

The universality of the reduced pressure in (3.12) can be used to write Maxwell's equal-area rule in reduced form,

$$\int_{\rho_{r,v}}^{\rho_{r,l}} \frac{P_{r,sat}(T_r) - P_r}{\rho_r^2} \, \mathrm{d}\rho_r = 0. \tag{3.13}$$

The coexistence density ratio ρ_l/ρ_v at a given reduced temperature T_r is therefore also universal. Deviation from these universal values can be rooted either in numerical artefacts or inconsistent thermodynamics of the model. For a consistent discretization in the sense of Lax's equivalence theorem (Lax & Richtmyer 1956), the former should be vanishing in the limit of a well-resolved simulation. The substance-agnostic form of the non-dimensional equations, i.e. the principle of corresponding states, allows us to probe convergence by systematically thickening the interface.

To probe the consistency with the principle of corresponding states in our model, we performed simulations for different values of the weak attraction parameter *a* of the van der Waals equation of state in (3.2). Reduced coexistence densities are shown in figure 3 for four different values of *a*. It is observed that, down from the critical point to $T_r \approx 0.4$,
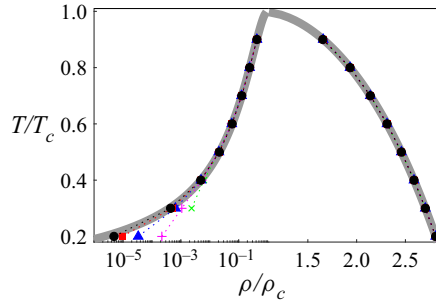
953 A4-16

Figure 3. Convergence to the principle of corresponding states. Coexistence densities as obtained from (grey lines) Maxwell's construction and (markers) simulations with different choices of a: (green $\times$) $a = 0.0102$; (magenta $+$) $a = 0.0051$; (blue triangles) $a = 0.0026$; (red squares) $a = 0.0013$ and (black circles) $a = 0.00064$.

coexistence densities essentially overlap for all the four values of a, in agreement with the principle of corresponding states. Deviations from the principle of corresponding states are most pronounced on the vapour side, as observed in figure 3. This can be explained as follows. The local value of the scaling parameter ε in (2.72) is estimated as $\varepsilon_{l,v} \sim \delta t \mathcal{F}/\rho_{l,v} \mathcal{U}$ in the liquid and in the vapour, respectively. Hence, their relative magnitude scales as the inverse of the density ratio, $\varepsilon_v/\varepsilon_l \sim \rho_l/\rho_v$. Thus, even if the scaling condition in (2.72) is satisfied for the liquid, $\varepsilon_l \ll 1$, it is still prone to violation for the vapour, if the density ratio ρ_l/ρ_v becomes sufficiently large. Conversely, if the scaling condition is satisfied for vapour, $\epsilon_v \ll 1$, it is also satisfied for liquid. Furthermore, due to the scaling relation between interface width and temperature detailed in § 3.6, the interface gets thinner at lower temperatures. This in turn means that for a given δr, fewer grid-points resolve the interface with decreasing temperature. Whenever the parameters $\delta r/W$ and $\delta t F/\rho \mathcal{U}$ increase, contributions of higher orders in ε become significant and lead to deviations from the analytical predictions. The characteristic interface width scales as $W \propto 1/\sqrt{a}$ (Jamet *et al.* 2001). As such, lower values of a lead to larger W, in parallel with smaller force increments over δt, which restores dominance of order ε terms over Burnett and super-Burnett level contributions, and therefore the corresponding states principle. This last point is demonstrated by the convergence of the coexistence density ratio to the analytical predictions with decreasing a. For well-resolved simulations, as shown in figure 2, the model correctly recovers the coexistence densities and thus complies with the principle of corresponding states. Below, we refer to the convergence of the scheme to the principle of corresponding states as the thermodynamic convergence.

To further clarify the utility of the principle of corresponding states in probing convergence, we have also conducted simulations similar to those reported in figure 3, with the first-neighbour pseudo-potential model (Shan & Chen 1993), (2.70), supplemented with the van der Waals equation of state (Yuan & Schaefer 2006). The results are shown in figure 4. Two points are worth noting here. First, a notion of convergence is present as co-existence densities do converge to a limit. However, *that* limit does not correspond to the capillary fluid model. Deviations become pronounced at lower temperatures where density ratios are larger. These differences are explained by the thermodynamic consistency issue where the mechanical stability condition governing the classical pseudo-potential model is recovered as (Benzi *et al.* 2006; Shan 2008)

$$\int_{\rho_{r,v}}^{\rho_{r,l}} (P_{r,sat}(T_r) - P_r) \frac{1}{\psi_r^2} \frac{\partial \psi_r}{\partial \rho_r} \, \mathrm{d}\rho_r = 0, \tag{3.14}$$
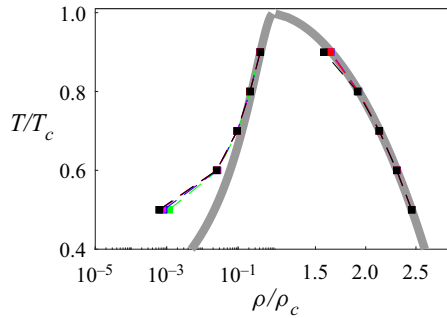
953 A4-17

Figure 4. Coexistence densities as obtained from (grey lines) Maxwell's construction and (markers) simulations with different choices of a: (green $\times$) $a = 0.0102$; (magenta $+$) $a = 0.0051$; (blue triangles) $a = 0.0026$; (red squares) $a = 0.0013$ and (black circles) $a = 0.00064$. Simulations are conducted using the first-neighbour pseudo-potential model in (2.70).

which is different from (3.13). Here $\psi_r = \psi/\psi_c$, where ψ_c is the pseudo-potential at critical state. This in turn naturally leads to observations of figure 4 where the discrete solver is convergent, but to a continuum-level behaviour dictated by (3.14) rather than the capillary fluid of (3.13). It is worth nothing that a number of numerical modifications have been proposed to improve on this issue. A detailed overview of such changes is out of the scope of the present work. Interested readers are referred to Chen *et al.* (2014) for a review.

3.3. *Temperature dependence of the surface tension near the critical point*

Surface tension at the liquid–vapour interface decreases with increasing temperature and vanishes at the critical point (Guggenheim 1945). For the van der Waals equation of state, the surface tension coefficient σ follows a scaling law as $T_r \to 1$ (van der Waals 1894; Blokhuis & Kuipers 2006),

$$\sigma = \frac{16a}{27b^2}\sqrt{\frac{\kappa}{a}}(1 - T_r)^{3/2}. \tag{3.15}$$

To probe the consistency of the proposed lattice Boltzmann model, the temperature dependence of the surface tension was numerically measured in two different configurations, the flat interface and the circular drop, in a temperature interval $T_r \in [0.85, 1]$.

In the first configuration, the surface tension coefficient was evaluated using its definition for the flat interface (Kirkwood & Buff 1949),

$$\sigma = \int_{-\infty}^{+\infty}(P_{xx} - P_{yy})\,\mathrm{d}x, \tag{3.16}$$

where the interface is normal to the x-axis in a two-dimensional simulation setup. The normal P_{xx} and the tangential P_{yy} components of the discrete pressure tensor were computed using a formalism developed in Appendix E, following a proposal by Shan (2008).

In the second configuration, simulations of circular liquid drops surrounded with vapour at the centre of a square domain were conducted. At each temperature, four different initial drop radii were considered, $R_0 \in \{45, 55, 65, 75\}$, chosen in such a way that the interface width is sufficiently small compared to the initial drop radius. In the simulation, we used

$W/R_0 \leq 0.1$, where $W = (\rho_l - \rho_v)/\max|\nabla\rho|$ is the interface width, to minimize the curvature dependence of surface tension. The corresponding surface tension coefficient was evaluated using the Laplace law ($D = 2$) in a form,

$$\Delta P = \frac{(D - 1)\sigma}{R_e}, \tag{3.17}$$

where the radius R_e corresponds to the *equimolar* dividing surface (Gibbs 1874).

A brief reminder of Gibbs' theory of dividing surfaces is in order. The total mass in both the diffuse and sharp interface pictures can be written as

$$\int_V \rho \, \mathrm{d}V = \rho_l V_l + \rho_v V_v + \Gamma, \tag{3.18}$$

where $\rho_l V_l$ and $\rho_v V_v$ are the masses in the bulk liquid and vapour phases in the sharp interface picture, while Γ is the excess mass on a dividing surface Σ, or mass *adsorbance* (Gibbs 1874). By requiring that no mass be stored on the dividing surface, we get the definition of the *equimolar* surface,

$$\Gamma = 0. \tag{3.19}$$

The family of dividing surfaces in the case of drop or bubble are concentric spheres ($D = 3$) or concentric circles ($D = 2$) parametrized by their radius R. In particular, for a two-dimensional drop, the mass adsorbance can be written as a function of the radius of the dividing circle,

$$\Gamma(R) = \int_0^{2\pi} \int_0^\infty (\rho(r) - \rho_v)r \, \mathrm{d}r \, \mathrm{d}\varphi - \int_0^{2\pi} \int_0^R (\rho_l - \rho_v)r \, \mathrm{d}r \, \mathrm{d}\varphi, \tag{3.20}$$

while the zero-adsorption condition in (3.19), $\Gamma(R_e) = 0$, implies the equimolar radius R_e,

$$R_e = \sqrt{\frac{\displaystyle\int_0^\infty (\rho(r) - \rho_v)r \, \mathrm{d}r}{(\rho_l - \rho_v)}}. \tag{3.21}$$

The drop configuration along with the scaling of the pressure difference across the interface with drop radius are shown in figure 5.

The results as obtained from both the flat interface and the drop configurations are shown in figure 6. It is clearly observed that the surface tensions as obtained from the proposed formulation (using either one of the considered configurations) agree very well with (3.15), provided that $W \ll R_e$. Discussion of the curvature dependence of surface tension shall be continued in § 3.5.

3.4. *Control of surface tension*

The present formulation allows us to select the surface tension in the simulation via the capillarity parameter κ, independently from the density ratio and temperature. To demonstrate this feature, flat interface simulations were performed at three reduced temperatures, $T_r = \{0.99, 0.98, 0.97\}$, for different values of $\tilde{\kappa}$. The surface tension was evaluated using (3.16). Results in figure 7 demonstrate that the surface tension can be effectively tuned using $\tilde{\kappa}$ and that changes in surface tension do not affect the equilibrium density ratios. This is further detailed in table 1 where the values of surface tension and deviations of the vapour and liquid densities from theoretical values are given as a function
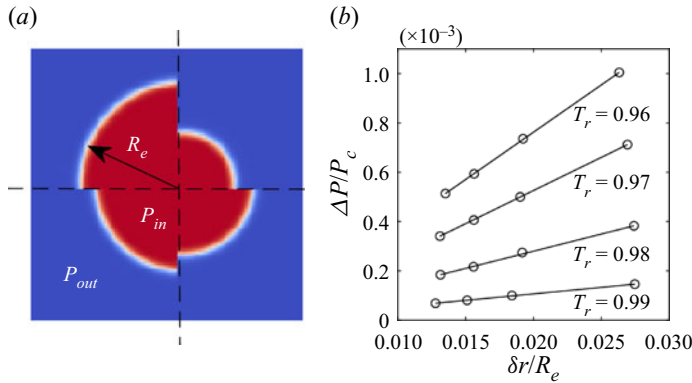
Figure 5. (*a*) Circular $D = 2$ drop configurations; (*b*) pressure difference scaling with drop radius for $T_r = 0.99, 0.98, 0.97$ and 0.96. The pressure difference is defined as $\Delta P = P_{in} - P_{out}$. The slope of the straight line is the surface tension coefficient.
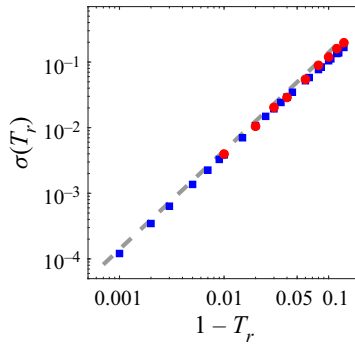

Figure 6. Temperature dependence of the surface tension coefficient near the critical point. Dashed grey line, theory using (3.15); red circles, simulation results using Laplace's law in (3.17); blue squares, surface tension coefficient computed by (3.16).

of $\tilde{\kappa}$ for $T_r = 0.97$. It is clearly observed that while the surface tension covers two orders of magnitude, the deviation from the predicted density of vapour is at most 0.041 percent. Furthermore, in the limit of vanishing κ, the surface tension also vanishes, as expected from the theory, (3.15).

3.5. *Effect of curvature on surface tension: Tolman length*

The drop simulation in §3.3 made use of the Laplace law, relying on the equimolar dividing surface of radius R_e in (3.21). Further discussion on the non-uniqueness of the choice of the dividing surface and the curvature dependence of surface tension is in order. Following Gibbs (1874), the free energy of a drop or bubble separated from the surrounding vapour or liquid by a dividing circle ($D = 2$) or sphere ($D = 3$) of length or area Σ is $A = U - TS + \sigma \Sigma$, where U and S are the internal energy and entropy of bulk phases while the last term is the adsorbance of free energy. The equilibrium condition requires vanishing of the variation δA; for the isothermal case, we have

$$\delta A = -P_{l,v}\delta V_{l,v} - P_{v,l}\delta V_{v,l} + \Sigma \delta \sigma + \sigma \delta \Sigma = 0, \tag{3.22}$$
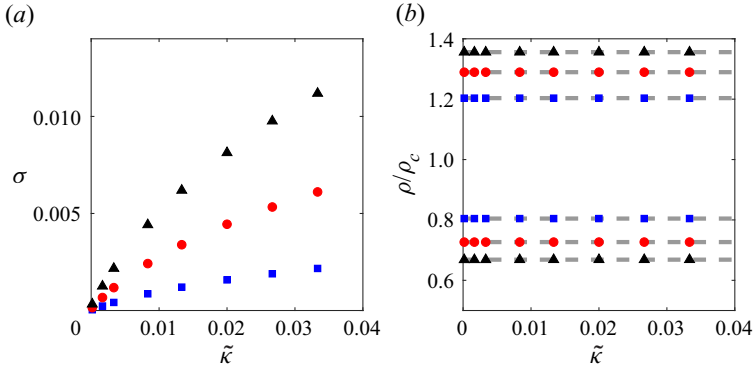
(*a*)   (*b*)

Figure 7. (*a*) Surface tension as a function of capillarity parameter $\tilde{\kappa}$; (*b*) liquid/vapour densities as a function of $\tilde{\kappa}$. Results of simulation shown at three different reduced temperatures: blue square, $T_r = 0.99$; red circles, $T_r = 0.98$; black triangles, $T_r = 0.97$. Dashed grey lines, theoretical coexistence densities from the Maxwell construction.

$\tilde{\kappa} \times 10^3$	0.2	1.7	3.3	8.3	13.3	20	26.7	33.3
$\sigma \times 10^2$	0.03	0.13	0.22	0.44	0.62	0.81	0.98	1.12
$\frac{\lvert \Delta \rho_v \rvert}{\rho_v} \times 10^3$	0.41	0.33	0.27	0.15	0.1	0.06	0.04	0.03
$\frac{\lvert \Delta \rho_l \rvert}{\rho_l} \times 10^3$	0.11	0.09	0.08	0.04	0.03	0.02	0.01	0.009

Table 1. Effect of the choice of $\tilde{\kappa}$ on surface tension and deviations in equilibrium vapour and liquid phases densities for $T_r = 0.97$.

where $P_{l,v}$ and $P_{v,l}$ are the pressures inside and outside the liquid drop or vapour bubble. Using $\delta V_{l,v} = -\delta V_{v,l} = 2(D-1)\pi R^{D-1} \delta R$ and $\delta \Sigma = 2(D-1)^2 \pi R^{D-2} \delta R$ leads to a generalized Laplace law,

$$\Delta P = \frac{(D-1)\sigma(R)}{R} + \frac{\mathrm{d}\sigma(R)}{\mathrm{d}R}. \tag{3.23}$$

The derivative of surface tension $\mathrm{d}\sigma/\mathrm{d}R$ is termed a *notional* derivative by some authors (Blokhuis & Bedeaux 1992) to stress that it refers to arbitrariness of the dividing surface. Apart from the equimolar surface in (3.21), the *surface of tension* is another possible choice to lift the ambiguity of the dividing surface. The notional derivative vanishes at the surface of tension,

$$\left. \frac{\mathrm{d}\sigma}{\mathrm{d}R} \right|_{R=R_s} = 0, \tag{3.24}$$

thereby reducing the generalized Laplace law in (3.23) to a standard form,

$$\Delta P = \frac{(D-1)\sigma(R_s)}{R_s}. \tag{3.25}$$

Integrating (3.23) from R_s to R, and eliminating ΔP using (3.25), one obtains an analytic expression for the notional surface tension $\sigma(R)$ relative to its minimum σ_s at the surface
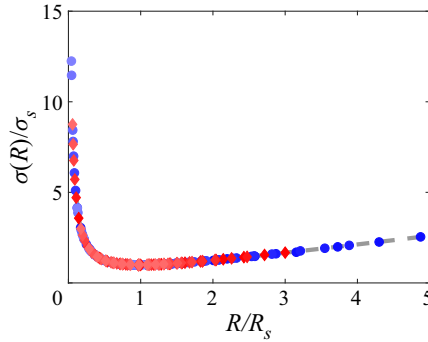
953 A4-21

Figure 8. Variation of surface tension σ with the radius of the dividing circle R at $T_r = 0.98$. Grey dashed line, theory in (3.26); symbol, simulations with van der Waals equation of state; blue circles, drop simulations; red diamonds, bubble simulations. Shading from dark to light, drops and bubbles of increasing sizes are shown.

of tension R_s,

$$\frac{\sigma(R)}{\sigma_s} = \frac{1}{D}\left(\frac{R_s}{R}\right)^{D-1} + \frac{D-1}{D}\left(\frac{R}{R_s}\right). \tag{3.26}$$

Equation (3.26) provides for a simple way of identifying the surface of tension and the corresponding surface tension. Two-dimensional simulations at $T_r = 0.98$ were conducted with different initial drop and bubble sizes, $R_0 \in \{30, 40, 50, 60, 70, 80, 100, 120, 140\}$. For each dividing surface of radius R, the corresponding surface tension was evaluated as (Blokhuis & Bedeaux 1992)

$$\sigma(R) = \int_0^\infty \left(\frac{r}{R}\right)^{D-1}[P_\perp(r, R) - P_\parallel(r)]\,\mathrm{d}r, \tag{3.27}$$

where $P_\parallel(r)$ is the tangential component of the pressure tensor, computed via the discrete pressure tensor detailed in Appendix E, and

$$P_\perp(r, R) = P_{in} - (P_{out} - P_{in})H(r - R) \tag{3.28}$$

is the normal pressure component in the sharp interface system, where H is the Heaviside step function. For each drop or bubble, surface tension $\sigma(R)$ in (3.27) was probed at seventeen equidistant dividing circles between $R_{min} = 5\delta r$ and $R_{max} = 165\delta r$. The discrete values $\sigma(R)$ obtained in these simulations were fitted with (3.26), with σ_s and R_s as the free fitting parameters. Figure 8 shows that the data for all drops and bubbles collapsed on a single master curve are in excellent agreement with the theory in (3.26). Thus, the proposed model correctly identifies the surface of tension for the van der Waals fluid.

While the notional derivative $\mathrm{d}\sigma(R)/\mathrm{d}R$ vanishes at the surface of tension, the same does not hold for the surface tension *at* the surface of tension, $\mathrm{d}\sigma_s/\mathrm{d}R_s \neq 0$. In other words, surface tension σ_s depends on the curvature of the surface of tension. In a seminal paper, Tolman (1949) characterized the curvature dependence of surface tension by the Tolman length. For sufficiently large R_s, the leading-order curvature dependence of the surface tension may be written as (Tolman 1949)

$$\sigma(R_s) \approx \sigma_0\left(1 \mp \frac{(D-1)\delta_T}{R_s}\right), \tag{3.29}$$

where δ_T is the Tolman length and σ_0 is the flat interface surface tension coefficient. Here, the negative (positive) sign corresponds to drops (bubbles).
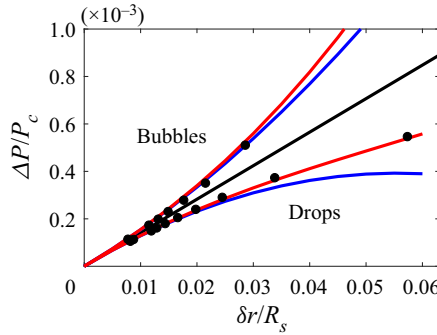
953 A4-22

Figure 9. Pressure difference scaling with surface of tension radius R_s for liquid drops and vapour bubbles. Symbol, simulation data for van der Waals equation of state with $a = 0.18$ and $b = 0.095l$; black line, Laplace law with $\sigma = \sigma_0$; blue lines, best fit with (3.29) used to compute Tolman length δ_T; red lines, best fit with the second-order Helfrich expansion in (3.30).

We first compare the leading-order Tolman model in (3.29) with the simulation. The values of R_s obtained in the previously described drops and bubbles simulations of figure 8 are plotted against the pressure difference for different drop and bubble sizes in figure 9. It is clear that for smaller drops and bubbles, the pressure difference deviates from the Laplace law with constant $\sigma_s = \sigma_0$, indicating a curvature-dependent surface tension. Fitting the data points with (3.29), the Tolman length can be extracted from the simulation, here $\delta_T = 9\delta r$ for both drops and bubbles, at the reduced temperature $T_r = 0.98$.

While the leading-order Tolman correction in (3.29) improves the agreement with data at moderate R_s, deviation persists for smaller drops and bubbles at $\delta r/R_s > 0.03$. Higher-order terms in the inverse powers of R_s, important for droplets or bubbles of small radius, are neglected by (3.29) and are addressed by Helfrich (1978)

$$\sigma = \sigma_0 \mp \sigma_0 \frac{(D-1)\delta_T}{R_s} + \frac{k(D-1)^2}{2R_s^2} + \frac{\bar{k}(D-2)}{R_s^2} + \cdots, \tag{3.30}$$

where k and $\bar{k}$ are the bending and Gaussian rigidities; note that the latter vanishes for $D = 2$. Taking the second-order term in (3.30) into account, the best fit in figure 9 results in bending rigidity $k = 1.049 \times 10^5 \sigma_0 \delta r^2$.

Finally we consider the limit of a flat interface where the Tolman length can be derived independently from the above considerations. In this case, the location of the surface of tension X_s can be found as the normalized first-order moment of the normal stress difference (Rao & Berne 1979),

$$X_s = \frac{\displaystyle\int_{-\infty}^{\infty} x(P_{xx} - P_{yy})\,dx}{\displaystyle\int_{-\infty}^{\infty} (P_{xx} - P_{yy})\,dx}. \tag{3.31}$$

With the dividing surface as a vertical straight line at X in two dimensions, the mass adsorbance $\Gamma(X)$ is defined as (see example in figure 10)

$$\Gamma(X) = \int_{-\infty}^{\infty} [\rho(x) - \rho_v - (\rho_l - \rho_v)H(x - X)]\,dx. \tag{3.32}$$

Similar to the case of cylindrical symmetry considered in § 3.3, the equimolar surface is found by annihilating the mass adsorbance, $\Gamma(X_e) = 0$.
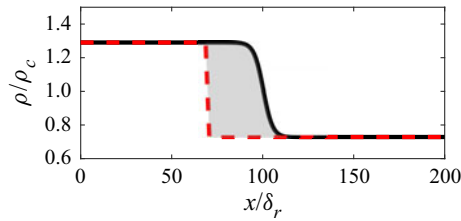
Figure 10. Example of mass adsorbance for a flat interface. Black continuous line, density profile at $T_r = 0.98$; red dashed line, sharp interface profile with the dividing surface at $X/\delta r = 70$. Grey area represents the mass adsorbance $\Gamma(X)$ in (3.32).
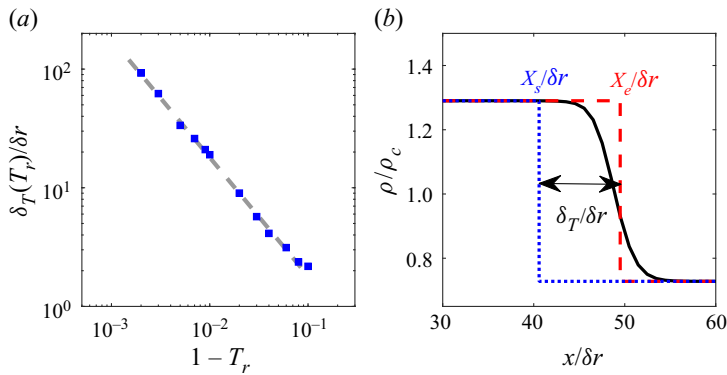

Figure 11. (*a*) Temperature dependence of Tolman length δ_T. Results from the flat interface simulation for van der Waals fluid are shown with blue squares while the grey dashed line represents theoretical scaling by (3.34). (*b*) Surface of tension, equimolar surface and Tolman length for a flat interface. Continuous black line, density profile at $T_r = 0.98$; red dashed line, sharp approximation with the equimolar surface as the dividing surface; blue dotted line, sharp approximation with the surface of tension as the dividing surface. Distance between the surface of tension and the equimolar surface is the Tolman length. In all simulations, $a = 0.18$ and $b = 0.095$.

The Tolman length in the limit of the flat interface is the distance between the surface of tension and the equimolar surface (Blokhuis & Bedeaux 1992; Blokhuis & Kuipers 2006),

$$\delta_T = X_e - X_s. \tag{3.33}$$

An example from the simulation is presented in figure 11. As shown by Blokhuis & Bedeaux (1992), the Tolman length scales with the reduced temperature as

$$\delta_T \propto (1 - T_r)^{-1}. \tag{3.34}$$

To validate the scaling of (3.34) in our model, flat interface simulations were conducted over a range of temperatures in the vicinity of the critical state. The Tolman length in (3.33) for various temperatures is shown in figure 11. The results obtained from simulations are in excellent agreement with the theoretical scaling by (3.34). A similar study using the Shan–Chen equations of states and the pseudo-potential model was presented in (Lulli *et al.* 2021). Furthermore, the flat interface simulations lead to a $\delta_T = 9.2\delta r$ at $T_r = 0.98$, in agreement with the value obtained from drop and bubble simulations, $\delta_T = 9\delta r$ at the same temperature. The relatively small discrepancy can be attributed to higher-order terms in the curvature, neglected in the fitting process.

953 A4-24

3.6. *Interface width: temperature scaling and control*

In the present work, we use a definition for the interface width bearing numerical information as to how well the stiff gradients are resolved on a given mesh, making it directly related to the velocity increment per time step:

$$W = \frac{\rho_l - \rho_v}{\max|\nabla \rho|}, \tag{3.35}$$

where ρ_l and ρ_v are the densities of saturated liquid and vapour, respectively. It can readily be observed that in the limit of a sharp interface, i.e. resolved with δr, $\delta r/W \to 1$. As previously noted for the co-existence densities and surface tension, the model recovers thermodynamical properties/scalings of the second-gradient fluid in the limit $\varepsilon \to 0$, akin to $\delta r/W \to 0$. As such, in the limit of $\delta r/W \to 1$, one expects numerical effects to dominate and observe deviations from thermodynamics of the van der Waals fluid.

Surface tension vanishes as the temperature approaches the critical, cf. § 3.3, (3.15) and figure 6, while the interface diverges as $T \to T_c$. As noted by Widom (1965), the van der Waals theory predicts the temperature scaling of the interface width as

$$W(T_r) \propto (1 - T_r)^{-1/2}. \tag{3.36}$$

To validate the consistency of the proposed model, simulations of flat interfaces were carried out in a range of reduced temperatures T_r near the critical point, and corresponding interface widths $W(T_r)$ in (3.35) were measured. Given the effect of the choice of a on interface thickness, simulations were also carried out with different a. The results obtained from simulations near the critical point are shown in figure 12. As noted by many authors in the literature (Jamet *et al.* 2001), the parameter a can be used to control the interface thickness, as done in the present work, at a given density ratio, leaving the ratios and Maxwell construction unaffected. In agreement with the equivalent states theory, the right-hand side plot in figure 12 points to the universality of the scaling of the interface width near the critical point regardless of the choice of a. In addition, it is interesting to note that for a fixed grid-size δr, as $(1 - T_r) \to 1$, $\delta r/W \to 1$ (equivalent to the scaling parameter ε introduced in the multi-scale analysis), indicating deviation from the thermodynamically converged state. This is illustrated by the deviation of the numerical interface thickness, starting at $T_r \approx 0.98$ from the theoretical predictions. Lowering the value of a, i.e. rescaling the interface by a factor $1/\sqrt{a}$ and therefore lowering ε, it is observed that interface is again well resolved and the scaling in (3.36) is restored. In agreement with previous sections, in the limit of $\varepsilon \to 0$, the model is shown to be thermodynamically converged and recovers the properties of the second-gradient fluid.

4. Hydrodynamic consistency

4.1. *Shear stress: layered Poiseuille flow*

The setup consists of a rectangular domain filled with the liquid phase at the bottom and the vapour phase on top. The flow is driven by a body force. Top and bottom are subject to no-slip boundary conditions while the inlet and outlet are fixed by periodicity. The momentum balance at the steady state reduces to a well-posed system of ordinary differential equations,

$$\partial_y \mu_l \partial_y u + \rho_l g = 0, \quad \forall y : 0 \le y \le h_l, \tag{4.1a}$$

$$\partial_y \mu_v \partial_y u + \rho_v g = 0, \quad \forall y : h_l \le y \le H, \tag{4.1b}$$
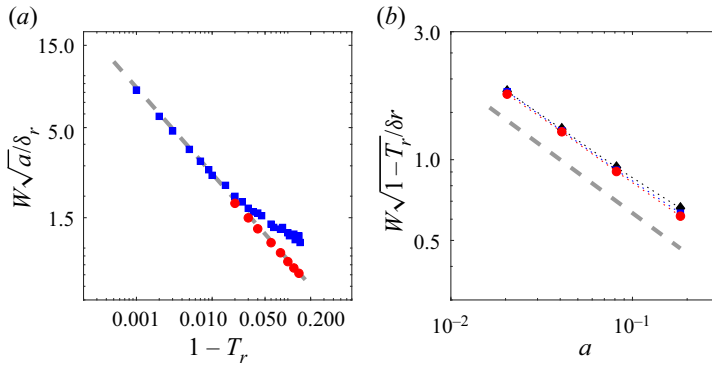
Figure 12. (*a*) Interface width as a function of temperature. Blue square, simulation with $a = 0.184$; red circle, simulation with $a = 0.02$; grey dashed line, theoretical scaling by (3.36). (*b*) Effect of the choice of a on the interface width. Simulation for $T_r = 0.98$ (diamond), 0.99 (square), 0.995 (circle).

closed by the following boundary conditions:

$$u|_{y=0} = 0, \tag{4.2a}$$

$$u|_{y=H} = 0, \tag{4.2b}$$

$$u|_{y=h_l^-} = u|_{y=h_l^+}, \tag{4.2c}$$

$$\mu_l \partial_y u|_{y=h_l^-} = \mu_v \partial_y u|_{y=h_l^+}. \tag{4.2d}$$

Here H is the height of the channel, h_l the height of the section filled with the liquid phase, μ_l and μ_v are the dynamic viscosities of the liquid and vapour, respectively, and g is the acceleration due to the body force. An analytical solution is given in Appendix F. This configuration is of particular interest as it probes the ability of a two-phase model to capture jump conditions at the interface which happens only if deviatoric components of the viscous stress tensor in (2.11) are correctly recovered.

Two sets of parameters were considered: (a) $\mu_l/\mu_v = 10.1$, $\rho_l/\rho_v = 10.1$ ($T_r = 0.77$) and (b) $\mu_l/\mu_v = 11.3$, $\rho_l/\rho_v = 1030$ ($T_r = 0.36$). Simulations were conducted on a grid of size 5×200, with a constant acceleration $g = 10^{-8} \delta r/\delta t^2$. Furthermore, the same simulations were performed with the conventional second-order equilibrium (Succi 2002) instead of the product form in (2.54). The steady-state results are compared to the analytical solution in figure 13. In contrast to the conventional second-order equilibrium, the use of the product form of (2.54) in our model recovers the correct jump conditions and therefore results in continuous velocity profiles, also for a large density ratio, in excellent agreement with analytical solution. A look at the maximum non-dimensional velocities in the domains, respectively 5×10^{-4} and 0.04 for density ratios 10 and 1000, further shows that in contrast to single-phase flows where deviations become only important for large non-dimensional velocities, here, due to the presence of large density gradients at the interfaces, third-order contributions to the equilibrium must be retained even for small velocities.

4.2. *Normal stress: dissipation of acoustic waves*

To assess Galilean invariance of the diagonal components of the viscous stress tensor and the effect of the correction term, the dissipation of acoustic waves was
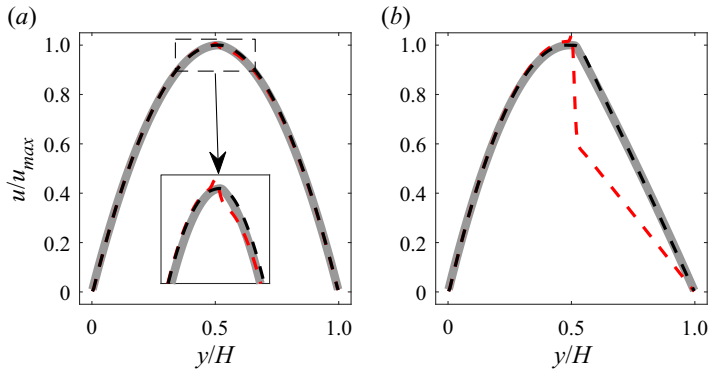
953 A4-26

Figure 13. Steady-state velocity profiles for the layered Poiseuille flow. Configuration (*a*) is where $T_r = 0.77$, $\rho_l/\rho_v = 10.1$, $\mu_l/\mu_v = 10.1$. Configuration (*b*) is where $T_r = 0.36$, $\rho_l/\rho_v = 1030$ and $\mu_l/\mu_v = 11.3$. Grey plain line, analytical solution; black dashed line, LBM with product-form equilibrium; red dashed line, LBM with conventional second-order equilibrium.

measured numerically. Acoustic waves were initialized as a small perturbation of density with an amplitude $\delta\rho$ and subject to uniform background velocity U_0 representing a moving reference frame,

$$\rho(x, 0) = \rho_0 + \delta\rho \sin(2\pi/\lambda), \tag{4.3}$$

where ρ_0 is the density of saturated liquid or vapour at a given temperature and λ is the wavelength of the perturbation. The maximum velocity in the domain was monitored over time and fitted to an exponential function of the form $\max(u) - U_0 = \exp(-\Lambda t)$, where the coefficient Λ is tied to the dissipation rate of the normal modes as

$$\eta = \frac{\Lambda}{(2\pi/\lambda)^2}. \tag{4.4}$$

Simulations were performed on a periodic domain of size $L = 128\delta r \times \delta r$ with $\lambda = 64\delta r$ at the temperature $T_r = 0.36$, corresponding to a density ratio $\rho_l/\rho_v \approx 10^3$. The perturbation amplitude was set to $\delta\rho = 10^{-4}\rho_0$ while the reference frame velocity varied in the range $U_0\delta t/\delta r \in [0, 0.3]$. The dissipation rate from (4.4) with and without the correction term are shown in figure 14. It is observed that the correction term for the third-order diagonal moments of the equilibrium populations in (2.58) restores the Galilean invariance (independence from the reference frame velocity) of the dissipation rate of normal modes.

4.3. *Viscosity-capillarity coupling: oscillating drop*

Rayleigh's classical study of a freely oscillating drop of non-viscous liquid under small deformations laid ground for the understanding of capillary waves (Rayleigh 1879). Assuming purely axisymmetric oscillation modes, Rayleigh's oscillation frequency of the nth mode, $n = 2, 3, \ldots$, for large density ratios, $\rho_l/\rho_v \gg 1$, is given by

$$f_n = \frac{1}{2\pi}\sqrt{\frac{\sigma n(n-1)(n+2)}{\rho_l R_0^3}}. \tag{4.5}$$

Two-dimensional simulations were performed for a drop of initial radius $R_0 = 40\delta r$, for a relatively low kinematic viscosity, $\nu_l\delta t/\delta r^2 = 0.01$. Modes of order $n = 2, 3, 4, 5, 6$
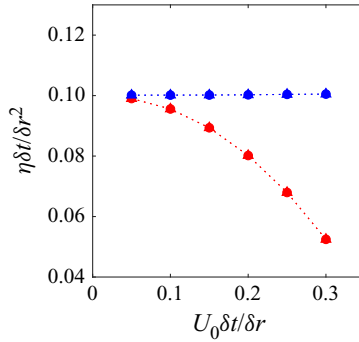
Figure 14. Dissipation rate of acoustic mode at $T_r = 0.36$. Circle, saturated liquid; triangle, saturated vapour. Blue, simulation of the model with the correction term; red, simulation of the model without the correction term.
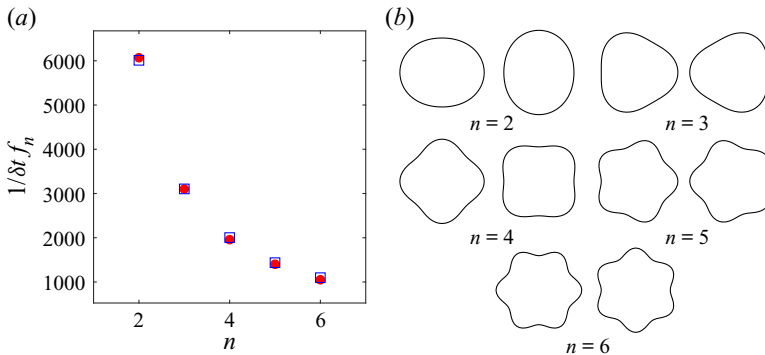

Figure 15. (*a*) Drop oscillation period for modes $n = 2, 3, 4, 5, 6$. Red circle, simulation; blue square, Rayleigh's modes from (4.5). (*b*) Corresponding shapes of the drop at $t = 1/2\delta t f_n$ and $t = 1/\delta t f_n$.

were initiated with a monochromatic perturbation, $R(\theta, 0) = R_0(1 + a_n \cos(n\theta) - \frac{1}{4}na_n^2)$, with the amplitude $a_n = 0.1$. The reduced temperature of the van der Waals fluid was set to $T_r = 0.36$, corresponding to a density ratio $\rho_l/\rho_v \approx 10^3$. The initial and mid-cycle shapes of Rayleigh's modes are shown in figure 15. Simulations were performed over eight oscillation cycles and corresponding oscillation periods were identified. Figure 15 demonstrates an excellent comparison of the oscillation frequencies measured in the simulation with the corresponding theoretical values from (4.5), even for higher-order modes. While Rayleigh's analysis was restricted to non-viscous liquids, a number of analytical solutions for viscous oscillating drops have been obtained over the years. In particular, Aalilija, Gandin & Hachem (2020) derived a time-dependent solution of the following form:

$$R(\theta, t) = R_0(1 + \epsilon_n \cos(n\theta) - \frac{1}{4}n\epsilon_n^2), \tag{4.6}$$

where $\epsilon_n = a_n \exp(-\lambda_n t) \cos(2\pi f_n t)$, while λ_n is the damping rate of the nth mode,

$$\lambda_n = 2n(n - 1)\nu_l R_0^{-2}. \tag{4.7}$$

To validate the damping rate of capillary waves, the previously described two-dimensional drop was simulated in a range of kinematic viscosities, $\nu_l \delta t/\delta r^2 \in [0.01, 0.1]$, subject to a monochromatic perturbation with the lowest mode $n = 2$ and the
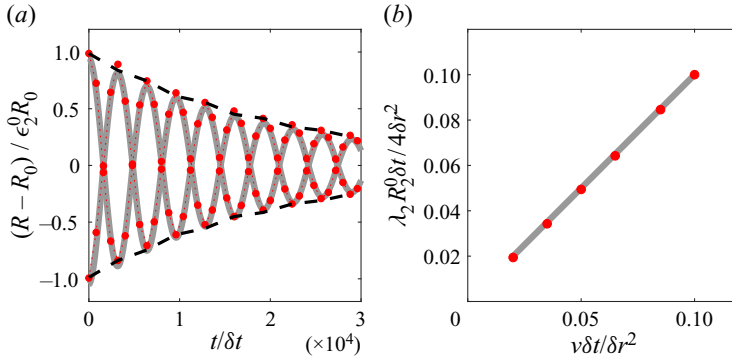
953 A4-28

Figure 16. (*a*) Time evolution of the drop radius in directions $\theta = 0$ and $\theta = \pi/2$ for kinematic viscosity $\nu\delta t/\delta r^2 = 0.02$. Grey line, analytical solution from (4.6); symbol: simulation; dashed black line, the $\exp(-\Lambda t)$ fit used to compute the dissipation rate in (4.7). (*b*) Apparent viscosity as computed via (4.7). Grey line, analytical solution from (4.7); symbol, simulation. All results correspond to the oscillation mode $n = 2$.

initial perturbation amplitude was set to $a_2 = 0.2$. The envelope of oscillations was fitted using the exponential function $\exp(-\Lambda t)$, see figure 16. The effective damping coefficient Λ was used along with (4.7) to evaluate the apparent kinematic viscosity. As shown in figure 16, the dissipation rates obtained by simulation agree well with the analytical solution from (4.7).

4.4. *Isothermal speed of sound*

Finally, we validate the speed of sound at different temperatures in both the liquid and vapour phases. For the van der Waals fluid, the isothermal sound speed is

$$c_s = \sqrt{\left.\frac{\partial P}{\partial \rho}\right|_T} = \sqrt{\frac{RT}{(b\rho - 1)^2} - 2a\rho}. \tag{4.8}$$

The sound speed was measured by monitoring the position of a pressure front over time in a quasi-one-dimensional simulation at different temperatures. The obtained results are compared to theory using (4.8) in figure 17. It is observed that the simulations accurately capture the speed of sound in both liquid and vapour phases, for the entire range of density ratios on the coexistence diagram in figure 2, up to at least $\rho_l/\rho_v \sim 10^{11}$. Results for other equations of state are compared in Appendix G.

4.5. *Interaction with solid boundaries: equilibrium contact angle*

A comprehensive review of various implementations of the contact angle on solid boundaries in the lattice Boltzmann setting can be found in Li *et al.* (2014). Here we follow a proposal by Benzi *et al.* (2006) where a virtual density, and therefore a corresponding virtual pseudo-potential, is attributed to the solid nodes. The calculations of the force using (2.69) are then carried at all fluid nodes. The no-slip condition is imposed via the modified bounce-back scheme of Bouzidi, Firdaouss & Lallemand (2001) for curved boundaries. The virtual density attributed to the solid nodes is the free parameters controlling the contact angle. The ability of this approach to correctly reproduce the dynamics of the contact line in a high-density ratio regime will be validated below.
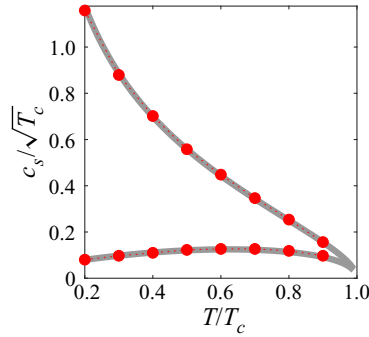
Figure 17. Isothermal sound speed for van der Waals fluid at various temperatures. Line, theory using (4.8); symbol, simulation. Upper branch, saturated liquid; lower branch, saturated vapour.

4.5.1. *Young–Laplace equation*

As a first validation of the solid/fluid interaction, the case of a two-dimensional channel of height H and length L is considered. Initially a rectangular column of liquid of length $L/3$ and height H surrounded by vapour was placed at the centre of the channel. Simulations were performed until the system reaches steady state, and the angle between the liquid/vapour interface and the solid wall at the triple-point was measured. The static contact angle measured at the triple-point should verify the Young–Laplace law for this configuration:

$$\Delta P = \frac{2\sigma \sin\theta}{H}, \qquad (4.9)$$

where θ is the equilibrium contact angle and σ the liquid/vapour surface tension.

Here, to validate the static angle, the reduced temperature of van der Waals fluid was set to $T_r = 0.36$, which corresponds to a density ratio $\rho_l/\rho_v = 10^3$. The height of the channel is set to $H = 75\delta r$ and the length to $L = 300\delta r$. The pressure difference ΔP is computed as the difference in pressure between two monitoring points located respectively inside and outside the liquid column. The convergence criterion used to assess steady state is based on the time variations of pressure at these two monitoring points. The contact angles were measured using the low-bond axisymmetric drop shape analysis module (Stalder *et al.* 2010) in ImageJ. The results obtained for the entire contact angle range are shown in figure 18. The measured contact angles show excellent agreement with the Young–Laplace equation. Furthermore, the results show that for $\rho_w \to \rho_v$, the contact angle tends to $\theta \to 180°$, while as $\rho_w \to \rho_l$, the contact angles tend to $\theta \to 0°$ therefore covering the entire range of contact angles.

4.5.2. *Wettability-driven drop motion in a channel*

A difference in contact angle on opposite sides of a liquid drop placed on a surface with a non-uniform wettability may initiate a motion of the drop. As a further validation of the solid/liquid interaction of the proposed model, the case of a liquid column placed in a channel and subjected to a wettability step function is considered. The configuration, illustrated in figure 19, consists of a channel of length L and width/height of H. Initially a liquid column of length L_l is placed at the channel centre. Once the liquid column has reached equilibrium, the wettability on the right-half of the channel is changed, which results in unequal contact angles on the different sides of the liquid column.
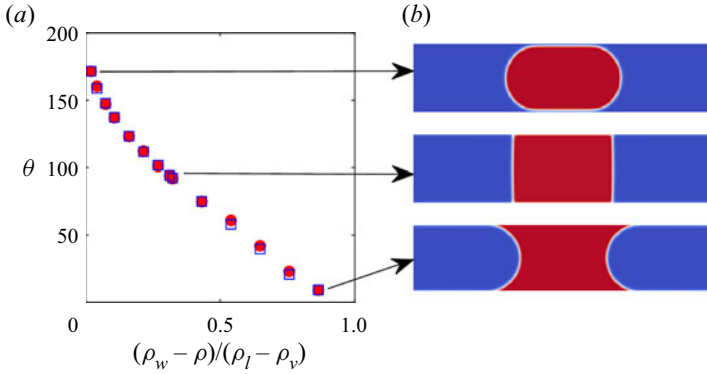
Figure 18. Static contact angles as (blue squares) obtained from the Young–Laplace equation and (red circles) measured directly from the simulations.
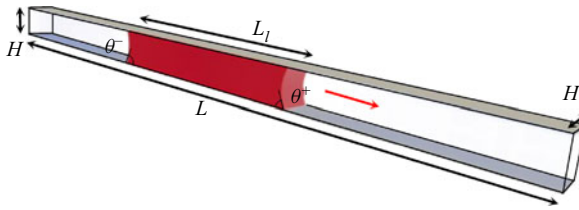

Figure 19. Schematics of the wettability-driven liquid column. Arrow indicates the direction of motion of the liquid column when the contact angle θ_+ (right) exceeds the contact angle θ_- (left).

An approximate analytical solution for the centre-of-mass position X and centroid velocity U was found by Esmaili, Moosavi & Mazloomi (2012),

$$X(t) = \tau_\infty U_\infty (e^{-t/\tau_\infty} + (t/\tau_\infty) - 1), \tag{4.10}$$

$$U(t) = U_\infty (1 - e^{-t/\tau_\infty}), \tag{4.11}$$

where the saturated centroid velocity U_∞ and transition time τ_∞ are computed respectively as

$$U_\infty = \frac{\sigma H (\cos\theta^- - \cos\theta^+)}{6[\rho_l \nu_l L_l + \rho_v \nu_v (L - L_l)]}, \tag{4.12}$$

$$\tau_\infty = \frac{H^2[\rho_l L_l + \rho_v (L - L_l)]}{12[\rho_l \nu_l L_l + \rho_v \nu_v (L - L_l)]}. \tag{4.13}$$

Here, $H = 70\delta r$ while $L = 1260\delta r$, $L_l = 420\delta r$, $\nu_l = \nu_v = 0.075\delta r^2/\delta t$ and the density ratio is set to 10^3 as in the previous cases. Initially, the contact angles on both sides of the water column were set to $\theta^- = 59.3°$. Once a steady state was reached, the contact angle on the right-hand side of the column was changed to $\theta^+ = 63.4°$, which resulted in a net force acting on the liquid. The liquid column centroid velocity and centre-of-mass position are compared to the analytical solutions in figure 20. Both quantities closely match analytical predictions.
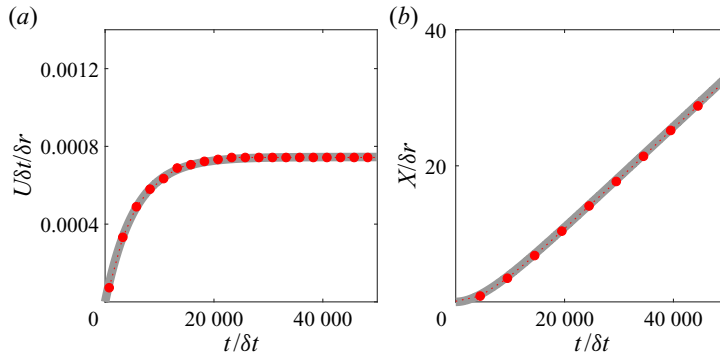
Figure 20. (*a*) Centroid velocity and (*b*) centre-of-mass position as obtained from (grey line) analytical solution and (red markers) LB simulations for the wettability-driven motion case.

5. Application to the dynamic cases

5.1. *Thermodynamic convergence and resolution requirements*

Two-phase lattice Boltzmann models are routinely used to simulate the impact of liquid drops on solids. While experiments are typically conducted with water and other liquids in air, the applicability of the two-phase LBM is justified whenever the dynamic effects are concerned. However, the majority of LB models do not reach the experimentally relevant density ratios of, say, the water/air density. The proposed LBM was demonstrated to be valid and thermodynamically well-posed at high density ratios. However, thermodynamic convergence, especially at higher density ratios comes at a cost in terms of interface resolution requirements. For instance, at $T_r = 0.36$ resulting in a density ratio of 10^3, to guarantee deviation below one percent from theory in the vapour phase, one must have $W > 8\delta r$. In large-scale hydrodynamic-dominated cases targeted in the present section, full thermodynamic convergence is not necessary. The only manifestations of deviation from the thermodynamically converged state that must be kept under control are spurious currents. Here, for density ratios 10^3, the interface thickness, in (3.35), is fixed at $W = 5\delta r$ resulting in a seven percent deviation of the vapour phase density from theory and spurious currents below $10^{-3}\delta r/\delta t$. The Tolman length for this choice of parameter is $\delta_T/\delta r = 2.4$ which, for the resolutions considered below ($R_0 = 75\delta r$), results in $\delta_T/R_0 = 0.032$ therefore minimizing the impact of curvature on effective surface tension. Below, we consider benchmark simulations of dynamic effects at realistic density ratios of increasing complexity to probe the accuracy and numerical stability of our model in the dynamic setting.

5.2. *Contact time on flat non-wetting surfaces*

Extensive studies of drop impact dynamics have shown that the contact time on so-called super-hydrophobic surfaces is independent of the Weber number, $We = \rho_l D_0 U_0^2/\sigma$, and only scales with the inertio-capillary time, $\tau_i = \sqrt{\rho_l D_0^3/8\sigma}$, i.e. for a given drop initial diameter D_0, the contact time is not affected by the impact velocity (Gauthier *et al.* 2015). The different stages of the impact process are illustrated in figure 21 through water drops impacting two surfaces with different contact angles. Simulations carried out under the same conditions are shown and already point to very good agreement between simulations and experiments. To quantify the ability of the proposed model to capture the dynamics of
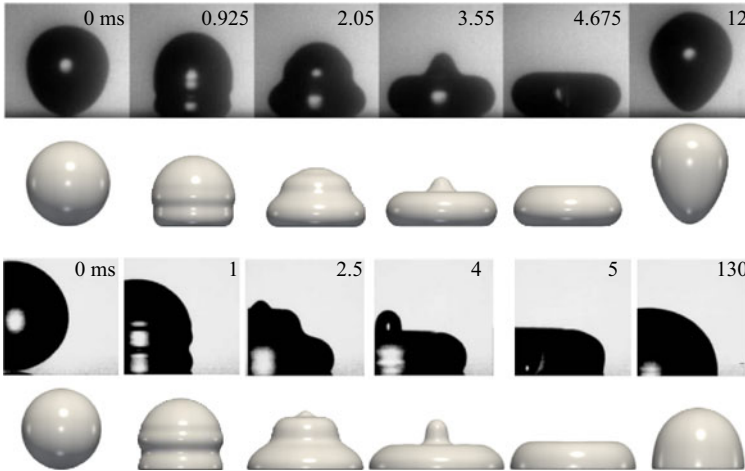
953 A4-32

Figure 21. Drop impacting flat solid surface with different contact angles (first and second row) $\theta = 180$ and (third and fourth row) $\theta = 90$. The Weber and Reynolds number are respectively 3.5 and 750. Experimental data from Vadillo *et al.* (2009) are shown in the first and third rows. Density ratios in both experiments and simulations are 10^3 and kinematic viscosity ratios are set to 15.
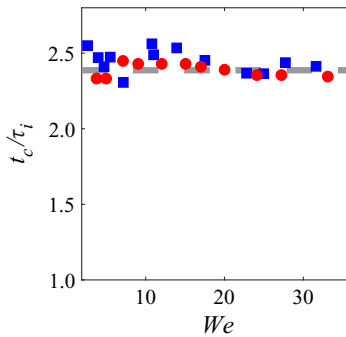

Figure 22. Drop contact times on flat non-wetting surface (contact angle $\theta = 165$ for different Weber numbers as obtained from simulations and experiments. Simulations results are shown with red circular markers while experimental data reported by Gauthier *et al.* (2015) are illustrated with blue square markers. The dashed grey line represents the average contact time as obtained from simulations, $\overline{t_c}/\tau_i = 2.4$.

drop impact and to investigate the Weber independence of the contact time on non-wetting surfaces, simulations were performed for a wide range of Weber numbers $We \in [1, 40]$, resulting in Reynolds numbers in the range of $Re \in [400, 1400]$, with $Re = U_0 D_0 / \nu_l$. Simulations have been performed in boxes of size $4D_0 \times 4D_0 \times 4D_0$ with $D_0 = 150\delta r$. The temperature was set to $T_r = 0.36$ resulting in a density ratio of 10^3. The obtained data show very good agreement with experimental contact times measured by Gauthier *et al.* (2015) and confirm the Weber independence of the contact times. Both numerical and experimental data are shown in figure 22.

5.3. *Reducing the contact time: pancake bouncing*

To further reduce the drop contact times, a number of different strategies have been devised during the past decades. Recently, Liu *et al.* (2014) proposed to use macroscopic structures, in the form of tapered posts, to reduce the contact time. It has been shown
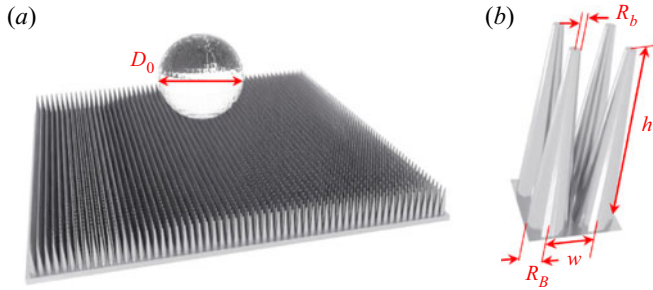
Figure 23. Illustration of the geometry of tapered posts. Configuration follows the experiment setup by Liu *et al.* (2014).

that above a certain threshold Weber number, these structures can decrease the contact time by approximately 75 %. This mechanism is also known as pancake bouncing, due to the pancake-like shape of the drop at take off. A detailed numerical study of pancake bouncing using LBM has been presented in (Mazloomi Moqaddam, Chikatamarla & Karlin 2017) for a limited range of densities. Here, to further demonstrate the versatility of our model, we consider a realistic density ratio of 10^3. The geometry consists of a flat substrate populated by tapered posts of base and tip radii R_B and R_b and height h with a centre-to-centre distance w in a simple square arrangement. The simulations were run following the geometrical configurations considered in experiments (Liu *et al.* 2014). Curved wall boundaries were implemented via the modified bounce-back scheme introduced by Bouzidi et al. (2001). The geometry is illustrated in figure 23. As for the flat substrate simulations, the domain size was set to $4D_0 \times 4D_0 \times 4D_0$ with $D_0 = 150\delta r$. Snapshots from the different stages of impact for two different Weber numbers, one below the pancake bouncing threshold and one above, from both simulations and experiments are shown in figure 24. The results show excellent agreement between simulations and experiments. The contact times for different Weber numbers, as obtained from simulations, are compared to the experimental results from Liu *et al.* (2014) in figure 25. It is shown that the numerical simulations not only accurately capture the contact time reduction due to pancake bouncing and the shape of the drop at take off, but they also correctly predict the onset of pancake bouncing. The shape of the drop at take off is assessed via the *pancake quality* parameter Q defined as the ratio of the drop radius at take off to its radius at maximum spreading (Liu *et al.* 2014).

5.4. *Extreme density ratios: inertia-dominated coalescence of mercury drops*

The sudden and pronounced topological changes involved in the coalescence of drops, especially the formation and subsequent evolution of the neck between them, have been of interest and subject to study for many years. The dynamics of the dimensionless neck radius r_{neck}/R_0 (with R_0 the drop's initial radius and r_{neck} the neck radius) have been shown to belong to one of two regimes (Eggers, Lister & Stone 1999) characterized by the Ohnesorge number, $Oh = \mu/\sqrt{2\rho_l\sigma R_0}$: highly viscous Stokes or inertial. The neck radius evolution over time has been shown to scale either as $r_{neck}/R_0 \propto t/\tau_i$ (in the viscous regime) or $r_{neck}/R_0 \propto \sqrt{t/\tau_i}$ (in the inertial regime). Here, to better illustrate the ability of the proposed scheme to model flows with extreme density ratios, we will focus on the first regime, more specifically, the coalescence of mercury droplets, with Ohnesorge numbers of the order of 10^{-4} (for 1 g drops). We consider a case following the experimental
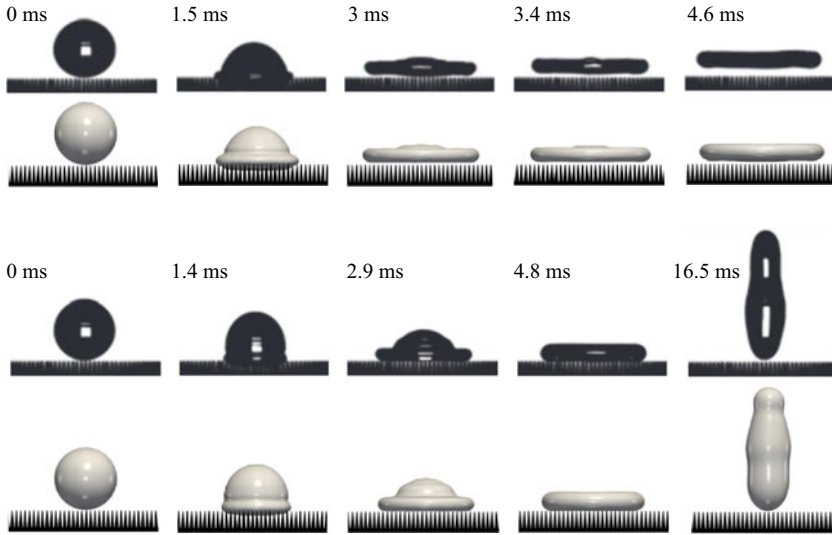
953 A4-34

Figure 24. Drop impacting tapered posts at different Weber numbers (first and second rows) $We = 28.2$ with pancake bouncing and (third and fourth rows) $We = 14.2$. The first and third rows are experiments from Liu *et al.* (2014) while the second and fourth rows are from simulations.
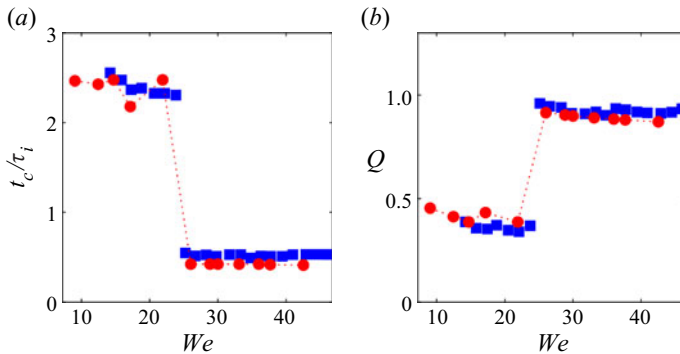

Figure 25. (*a*) Drop contact times and (*b*) pancake quality at rebound on tapered posts for different Weber numbers as obtained from simulations and experiments. Simulations results are shown with red circular markers while experimental data reported by Liu *et al.* (2014) are illustrated with blue square markers.

configuration of Menchaca-Rocha *et al.* (2001) with two 1 g mercury droplets. To match the proper density ratio of a mercury/air system ($\rho_{Hg} = 13\,600$ kg m^{-3}), the temperature is set to $T_r = 0.267$, resulting in a density ratio of $\rho_l/\rho_v \sim 11\,500$. The two drops, resolved with 150 points on their radii are placed in a rectangular domain of size $400 \times 400 \times 800$ with a centre-to-centre distance of 304 points. The drops are connected initially via a neck of 4-points radius. The evolution of the drops' shape over time are compared to experiments from Menchaca-Rocha *et al.* (2001) in figure 26. To further illustrate the agreement of numerical simulations with experiments, the evolution of the neck radii r_{neck} over time are shown in figure 27. Both qualitative comparison of the drops' shape and quantitative comparison of the neck radius show that the presented solver is able to correctly model multi-phase flow dynamics with extreme density ratio. To the best of
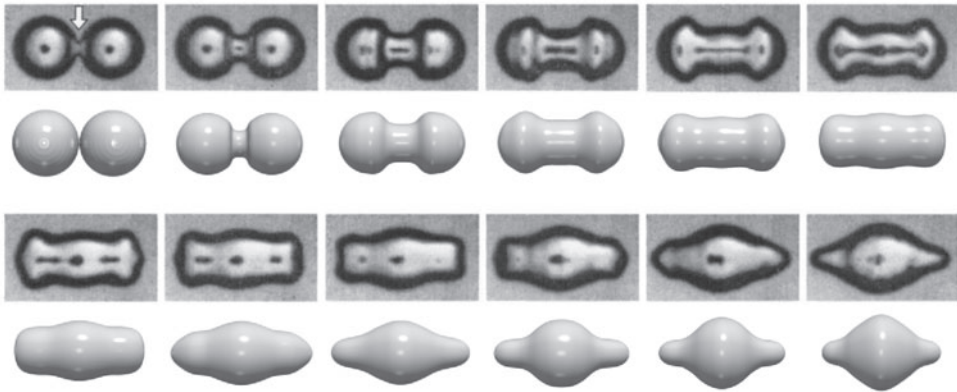
Figure 26. Sequential images from different stages of the mercury drops coalescence and sub-sequential capillary waves propagation. First and third-row images are from experiments of Menchaca-Rocha *et al.* (2001), while second and fourth rows are from LB simulations. Snapshots are taken at $\Delta t = 3.5$ ms intervals.
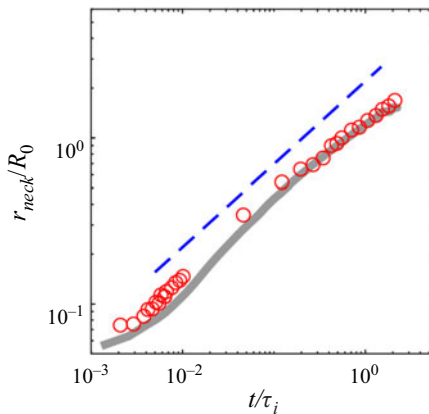

Figure 27. Time evolution of the neck radii from both (grey line) simulations and (red circular markers) experiments as reported by Menchaca-Rocha *et al.* (2001). The dashed blue line represents the $\sqrt{t/\tau_i}$ scaling with $\tau_i = \sqrt{\rho R_0^3/\sigma}$.

the authors' knowledge, this is the first lattice Boltzmann simulation at such high density ratios, regardless of the formulation, i.e. pseudo-potential, free energy, phase-field etc.

6. Conclusion

Multi-phase flows are a well-established area in kinetic theory and more specifically in the context of the LBM. While dynamic two-dimensional/three-dimensional simulations are routinely carried out with the different LB-based formulations, which are subject to continuous numerical *improvements*, a clear and concise kinetic framework along with a characterisation of the resulting fluid thermodynamic properties is lacking.

The aim of the present work was to develop a general framework for isothermal single-component multi-phase flow simulations consistent with the capillary fluid thermodynamics. Starting from the first-order BBGKY equation and using a projector operator in phase-space, a flexible model, in terms of pressure contribution partition,

is proposed. A specific realization of the partition minimizing deviations from the first-neighbour stencil reference (optimal) state was then discretized using the LBM. The discrete solver was shown to recover the full Navier–Stokes–Korteweg under the proposed scaling. The resulting discrete model was then probed for thermodynamic consistency and shown to abide by all the scaling laws of the corresponding meanfield, i.e. surface tension, interface thickness and Tolman length. Finally, the model was shown to allow for not only static, but dynamic large density ratios simulations with complex geometries, illustrated best by the extreme case of mercury drops coalescence, therefore effectively removing the well-known limitations on maximum density ratio.

The detailed study of the properties of the proposed model and accompanying theoretical analyses lead us to believe that the present framework fills important gaps in the multi-phase literature, more specifically in the context of discrete kinetic models such as the LBM. It provides a consistent framework for the simulation of challenging physics as demonstrated by the curvature dependence of the surface tension. Furthermore, it paves the way for extension to fully compressible non-ideal fluids and development of corresponding lattice Boltzmann solvers following our previously introduced compressible schemes (Saadat *et al.* 2021) which will be the topic of an upcoming publication.

Author ORCIDs.

 S.A. Hosseini https://orcid.org/0000-0003-4477-4289;

 I.V. Karlin https://orcid.org/0000-0001-9996-9679.

Appendix A. Short-range interaction

The non-local contributions to particle's interaction in (2.15) consist of short- and long-range interactions, and are classically treated by splitting the integral over physical space into two domains, $|r_1 - r| \leq d$ and $|r_1 - r| > d$, where d is the hard-sphere diameter. To derive the pressure form of the short-range interaction, we start with the Enskog hard-sphere collision integral (Enskog 1921; Chapman & Cowling 1939),

$$\mathcal{J}_E = d^2 \iint \left[\chi \left(r + \frac{d}{2}k \right) f(r, v') f(r + dk, v'_1) \right.$$
$$\left. - \chi \left(r - \frac{d}{2}k \right) f(r, v) f(r - dk, v_1) \right] g \cdot k \, dk \, dv_1, \quad (A1)$$

where $k = (r_1 - r)/|r_1 - r|$, $g = v_1 - v$, $v' = v + k(g \cdot k)$, $v'_1 = v_1 - k(g \cdot k)$ and χ is the equilibrium pair correlation function, evaluated at local density taking into account the effect of volume of particles in the collision probability (Chapman & Cowling 1939). Using a Taylor expansion around r,

$$\chi \left(r \pm \frac{d}{2}k \right) = \chi(r) \pm \frac{d}{2}k \cdot \nabla \chi(r) + O(d^2), \quad (A2)$$

$$f(r \pm dk, w) = f(r, w) \pm dk \cdot \nabla f(r, w) + O(d^2), \quad (A3)$$

and neglecting terms of order $O(d^4)$, the resulting approximation of the Enskog collision integral becomes

$$\mathcal{J}_E = \chi \mathcal{J}_B + \mathcal{J}_E^{(1)}, \tag{A4}$$

where $\mathcal{J}$ is the Boltzmann collision integral for hard-spheres,

$$\mathcal{J}_B = d^2 \iint [f(\boldsymbol{r}, \boldsymbol{v}') f(\boldsymbol{r}, \boldsymbol{v}'_1) - f(\boldsymbol{r}, \boldsymbol{v}) f(\boldsymbol{r}, \boldsymbol{v}_1)] \boldsymbol{g} \cdot \boldsymbol{k} \, \mathrm{d}\boldsymbol{k} \, \mathrm{d}\boldsymbol{v}_1, \tag{A5}$$

while $\mathcal{J}_E^{(1)}$ is the non-local contribution to the lowest order,

$$\mathcal{J}_E^{(1)} = d^3 \chi(\boldsymbol{r}) \iint \boldsymbol{k} \cdot [f(\boldsymbol{r}, \boldsymbol{v}') \nabla f(\boldsymbol{r}, \boldsymbol{v}'_1) + f(\boldsymbol{r}, \boldsymbol{v}) \nabla f(\boldsymbol{r}, \boldsymbol{v}_1)] \boldsymbol{g} \cdot \boldsymbol{k} \, \mathrm{d}\boldsymbol{k} \, \mathrm{d}\boldsymbol{v}_1$$
$$+ \frac{d^3}{2} \iint \boldsymbol{k} \cdot \nabla \chi(\boldsymbol{r}) [f(\boldsymbol{r}, \boldsymbol{v}') f(\boldsymbol{r}, \boldsymbol{v}'_1) + f(\boldsymbol{r}, \boldsymbol{v}) f(\boldsymbol{r}, \boldsymbol{v}_1)] \boldsymbol{g} \cdot \boldsymbol{k} \, \mathrm{d}\boldsymbol{k} \, \mathrm{d}\boldsymbol{v}_1. \tag{A6}$$

Since the Boltzmann collision integral conserves the mass and momentum locally, it is annulled by the projector,

$$\mathcal{K} \mathcal{J}_B = 0. \tag{A7}$$

Furthermore, $\mathcal{J}_{SR}^1$ is evaluated at the local equilibrium f^{eq} in (2.16) to get (Chapman & Cowling 1939)

$$\mathcal{J}_E^{(1)} = d^3 \iint f^{eq}(\boldsymbol{r}, \boldsymbol{v}) f^{eq}(\boldsymbol{r}, \boldsymbol{v}_1) \boldsymbol{k} \cdot \nabla \ln[\chi(\boldsymbol{r}) f^{eq}(\boldsymbol{r}, \boldsymbol{v}) f^{eq}(\boldsymbol{r}, \boldsymbol{v}_1)] \boldsymbol{g} \cdot \boldsymbol{k} \, \mathrm{d}\boldsymbol{k} \, \mathrm{d}\boldsymbol{v}_1, \tag{A8}$$

which, after integration in $\boldsymbol{v}_1$ and $\boldsymbol{k}$, for the isothermal flow, results in

$$\mathcal{J}_E^{(1)} = -b\rho \chi f^{eq} [(\boldsymbol{v} - \boldsymbol{u}) \cdot \nabla \ln \rho^2 \chi T]$$
$$- b\rho \chi f^{eq} \left[\frac{2}{5RT} (\boldsymbol{v} - \boldsymbol{u}) \otimes (\boldsymbol{v} - \boldsymbol{u}) : \nabla \boldsymbol{u} + \left(\frac{1}{5RT} |\boldsymbol{v} - \boldsymbol{u}|^2 - 1 \right) \nabla \cdot \boldsymbol{u} \right], \tag{A9}$$

where $b = 2\pi d^3 / 3m$. Finally, applying the isothermal projector $\mathcal{K}$, we obtain

$$\mathcal{K} \mathcal{J}_E^{(1)} = \frac{1}{\rho} \frac{\partial f^{eq}}{\partial \boldsymbol{u}} \cdot \int \boldsymbol{v} \mathcal{J}_E^{(1)} \, \mathrm{d}\boldsymbol{v}$$
$$= -\frac{1}{\rho} \frac{\partial f^{eq}}{\partial \boldsymbol{u}} \cdot \int \boldsymbol{v}(\boldsymbol{v} - \boldsymbol{u}) f^{eq}(\boldsymbol{r}, \boldsymbol{v}) \, \mathrm{d}\boldsymbol{v} \cdot \frac{b}{\rho T} \nabla \rho^2 \chi T$$
$$= -\frac{1}{\rho} \frac{\partial f^{eq}}{\partial \boldsymbol{u}} \cdot \nabla b \rho^2 \chi RT. \tag{A10}$$

While the phenomenological Enskog's collision integral (Enskog 1921) was used above, the lowest-order approximation in (A9) is identical in other versions of hard-sphere kinetic equations such as the revised Enskog theory (RET) (Van Beijeren & Ernst 1973) or kinetic variational theory (Karkheck & Stell 1981).

953 A4-38

Appendix B. Long-range interaction

Vlasov's mean-field approximation for a long-range interaction is reviewed next. Assuming the absence of correlations, the two-particle distribution function is approximated as

$$f_2(\boldsymbol{r}, \boldsymbol{v}, \boldsymbol{r}_1, \boldsymbol{v}_1) \approx f(\boldsymbol{r}, \boldsymbol{v}) f(\boldsymbol{r}_1, \boldsymbol{v}_1), \tag{B1}$$

while the long-range interaction integral can be simplified to

$$\mathcal{J}_V = \frac{\partial f(\boldsymbol{r}, \boldsymbol{v})}{\partial \boldsymbol{v}} \cdot \boldsymbol{\nabla} \left[\int_{|\boldsymbol{r}_1 - \boldsymbol{r}| > d} \rho(\boldsymbol{r}_1) V(|\boldsymbol{r}_1 - \boldsymbol{r}|) \, \mathrm{d}\boldsymbol{r}_1 \right]. \tag{B2}$$

With a Taylor expansion around $\boldsymbol{r}$,

$$\rho(\boldsymbol{r}_1) = \rho(\boldsymbol{r}) + (\boldsymbol{r}_1 - \boldsymbol{r}) \cdot \boldsymbol{\nabla}\rho(\boldsymbol{r}) + \tfrac{1}{2}(\boldsymbol{r}_1 - \boldsymbol{r}) \otimes (\boldsymbol{r}_1 - \boldsymbol{r}) : \boldsymbol{\nabla} \otimes \boldsymbol{\nabla}\rho(\boldsymbol{r}) + O(\nabla^3 \rho), \tag{B3}$$

and neglecting higher-order terms, (B2) leads to

$$\mathcal{J}_V = -\boldsymbol{\nabla}[2a\rho(\boldsymbol{r}) + \kappa\nabla^2\rho(\boldsymbol{r})] \cdot \frac{\partial}{\partial \boldsymbol{v}} f(\boldsymbol{r}, \boldsymbol{v}), \tag{B4}$$

where parameters a and κ are, after integration over a unit sphere,

$$a = -2\pi \int_d^\infty r^2 V(r) \, \mathrm{d}r, \tag{B5}$$

$$\kappa = -\frac{2\pi}{3} \int_d^\infty r^4 V(r) \, \mathrm{d}r. \tag{B6}$$

Applying the projector, we obtain

$$\begin{aligned}
\mathcal{K}\mathcal{J}_V &= \frac{1}{\rho} \frac{\partial f^{eq}}{\partial \boldsymbol{u}} \cdot \int \boldsymbol{v} \mathcal{J}_V \, \mathrm{d}\boldsymbol{v} \\
&= -\frac{1}{\rho} \frac{\partial f^{eq}}{\partial \boldsymbol{u}} \cdot \int \boldsymbol{v} \frac{\partial}{\partial \boldsymbol{v}} f(\boldsymbol{r}, \boldsymbol{v}, t) \, \mathrm{d}\boldsymbol{v} \cdot \boldsymbol{\nabla}[2a\rho + \kappa\nabla^2\rho] \\
&= \frac{\partial f^{eq}}{\partial \boldsymbol{u}} \cdot \boldsymbol{\nabla}[2a\rho + \kappa\nabla^2\rho].
\end{aligned} \tag{B7}$$

Finally, we can estimate the relative magnitude of the parameters a and κ by introducing a range of the attraction potential δ. Assuming $d \ll \delta$, we have $a \sim \bar{V}\delta^3$ and $\kappa \sim \bar{V}\delta^5$, where $\bar{V}$ is a characteristic value of the potential, and thus

$$\sqrt{\kappa/a} \sim \delta. \tag{B8}$$

Appendix C. Hydrodynamic limit of the Enskog–Vlasov–BGK kinetic model

C.1. *Rescaled kinetic equation*

For the Enskog–Vlasov–BGK kinetic model,

$$\partial_t f + \boldsymbol{v} \cdot \boldsymbol{\nabla} f = -\frac{1}{\tau}(f - f^{eq}) - \frac{1}{\rho} \frac{\partial f^{eq}}{\partial \boldsymbol{u}} \cdot [\boldsymbol{\nabla}(b\rho^2 \chi RT - a\rho^2) - \kappa\rho\boldsymbol{\nabla}\nabla^2\rho], \tag{C1}$$

let us introduce the following parameters: characteristic flow velocity $\mathcal{U}$; characteristic flow scale $\mathcal{L}$; characteristic flow time $\mathcal{T} = \mathcal{L}/\mathcal{U}$; characteristic density $\bar{\rho}$; isothermal

speed of sound of ideal gas $c_s = \sqrt{RT}$; kinematic viscosity of the BGK model of ideal gas $\nu = \tau c_s^2$. With the above, the variables are reduced as follows (primes denote non-dimensional variables): time $t = \mathcal{T}t'$; space $r = \mathcal{L}r'$; flow velocity $u = \mathcal{U}u'$; particle velocity $v = c_s v'$; density $\rho = \bar{\rho}\rho'$; distribution function $f = \bar{\rho}c_s^{-3}f'$. Furthermore, the following non-dimensional groups are introduced: viscosity-based Knudsen number $Kn = \tau c_s/\mathcal{L}$; Mach number $Ma = \mathcal{U}/c_s$; Enskog number $En = b\bar{\rho}Kn/Ma$; Vlasov number $Vs = a/bRT$. With this, the Enskog–Vlasov–BGK kinetic model is rescaled as follows:

$$Ma\, Kn\, \partial_t' f' + v' \cdot Kn\nabla' f' = -(f' - f^{eq'})$$

$$-\frac{1}{\rho'}\frac{\partial f^{eq'}}{\partial u'} \cdot En\left[\nabla'(\chi(\rho')^2 - Vs(\rho')^2) - \left(\frac{\delta}{\mathcal{L}}\right)^2 Vs(\rho'\nabla'\nabla'^2\rho')\right], \qquad \text{(C2)}$$

where δ is the range of the attraction potential, estimated according to (B8). The following scaling assumptions are applied: acoustic scaling, $Ma \sim 1$; hydrodynamic scaling, $Kn \sim En \sim \delta/\mathcal{L} \sim \epsilon$; Enskog–Vlasov parity, $Vs \sim 1$. In other words, the conventional hydrodynamic limit treats all non-dimensional groups that are inversely proportional to the flow scale $\mathcal{L}$ (Kn, En and $\delta/\mathcal{L}$) as a small parameter, while the Enskog–Vlasov parity ensures that both the short- and long-range contributions to the pressure are treated on equal footing. Returning to dimensional variables, we may write

$$\epsilon\partial_t f + v \cdot \epsilon\nabla f = -(f - f^{eq}) - \frac{1}{\rho}\frac{\partial f^{eq}}{\partial u} \cdot (\epsilon F^{(1)} + \epsilon^3 F^{(3)}), \qquad \text{(C3)}$$

where

$$F^{(1)} = \nabla(b\rho^2\chi RT - a\rho^2), \qquad \text{(C4)}$$

$$F^{(3)} = -\kappa\rho\nabla\nabla^2\rho. \qquad \text{(C5)}$$

Finally, taking into account the reference equilibrium in (2.34) and the reference pressure P_0, the rescaled kinetic equation in (2.35) takes the form of (C3) with

$$F^{(1)} = \nabla(P - P_0). \qquad \text{(C6)}$$

Chapman–Enskog analysis of the rescaled kinetic equation in (2.35) is presented in the next section.

C.2. *Chapman–Enskog analysis*

Expanding the distribution function as

$$f = f^{(0)} + \epsilon f^{(1)} + \epsilon^2 f^{(2)} + O(\epsilon^3), \qquad \text{(C7)}$$

introducing it back into (C3) and separating terms with different orders in ϵ, at order zero, one recovers

$$f^{(0)} = f^{eq}. \qquad \text{(C8)}$$

This latter implies the solvability conditions,

$$\int f^{(k)}\, dv = 0, \quad \forall k \neq 0, \qquad \text{(C9)}$$

$$\int v f^{(k)}\, dv = 0, \quad \forall k \neq 0. \qquad \text{(C10)}$$

At order ϵ:

$$\partial_t^{(1)} f^{(0)} + \boldsymbol{v} \cdot \boldsymbol{\nabla} f^{(0)} = -\frac{1}{\tau} f^{(1)} - \frac{1}{\rho} \frac{\partial f^{eq}}{\partial \boldsymbol{u}} \cdot \boldsymbol{F}^{(1)}, \tag{C11}$$

which, upon integration in $\boldsymbol{v}$, leads to

$$\partial_t^{(1)} \rho + \boldsymbol{\nabla} \cdot \rho \boldsymbol{u} = 0, \tag{C12}$$

$$\partial_t^{(1)} \rho \boldsymbol{u} + \boldsymbol{\nabla} \cdot \rho \boldsymbol{u} \otimes \boldsymbol{u} + \boldsymbol{\nabla} \cdot P_0 \boldsymbol{I} + \boldsymbol{F}^{(1)} = 0. \tag{C13}$$

At order ϵ^2:

$$\partial_t^{(2)} f^{(0)} + \partial_t^{(1)} f^{(1)} + \boldsymbol{v} \cdot \boldsymbol{\nabla} f^{(1)} = -\frac{1}{\tau} f^{(2)}, \tag{C14}$$

which leads to the following equation for mass conservation:

$$\partial_t^{(2)} \rho = 0, \tag{C15}$$

while for momentum:

$$\partial_t^{(2)} \rho \boldsymbol{u} + \boldsymbol{\nabla} \cdot \left[\int \boldsymbol{v} \otimes \boldsymbol{v} f^{(1)} \, d\boldsymbol{v} \right] = 0. \tag{C16}$$

The last term on the left-hand side can be evaluated using the previous order in ϵ as

$$\int \boldsymbol{v} \otimes \boldsymbol{v} f^{(1)} \, d\boldsymbol{v} = -\tau \left[\partial_t^{(1)} \int \boldsymbol{v} \otimes \boldsymbol{v} f^{(0)} \, d\boldsymbol{v} + \boldsymbol{\nabla} \cdot \int \boldsymbol{v} \otimes \boldsymbol{v} \otimes \boldsymbol{v} f^{(0)} \, d\boldsymbol{v} \right.$$
$$\left. + \frac{1}{\rho} \int \boldsymbol{v} \otimes \boldsymbol{v} \frac{\partial f^{eq}}{\partial \boldsymbol{u}} \cdot \boldsymbol{F}^{(1)} d\boldsymbol{v} \right], \tag{C17}$$

where

$$\partial_t^{(1)} \int \boldsymbol{v} \otimes \boldsymbol{v} f^{(0)} \, d\boldsymbol{v} = -\boldsymbol{\nabla} \cdot \rho \boldsymbol{u} \otimes \boldsymbol{u} \otimes \boldsymbol{u} - [\boldsymbol{u} \otimes (\boldsymbol{F}^{(1)} + \boldsymbol{\nabla} P_0) + (\boldsymbol{F}^{(1)}$$
$$+ \boldsymbol{\nabla} P_0) \otimes \boldsymbol{u}] + \partial_t^{(1)} P_0 \boldsymbol{I}, \tag{C18}$$

and

$$\boldsymbol{\nabla} \cdot \int \boldsymbol{v} \otimes \boldsymbol{v} \otimes \boldsymbol{v} f^{(1)} \, d\boldsymbol{v} = \boldsymbol{\nabla} \cdot \rho \boldsymbol{u} \otimes \boldsymbol{u} \otimes \boldsymbol{u} + [\boldsymbol{\nabla} P_0 \boldsymbol{u} + \boldsymbol{\nabla} P_0 \boldsymbol{u}^\dagger] + \boldsymbol{I} \boldsymbol{\nabla} \cdot P_0 \boldsymbol{u}, \tag{C19}$$

$$\frac{1}{\rho} \int \boldsymbol{v} \otimes \boldsymbol{v} \frac{\partial f^{eq}}{\partial \boldsymbol{u}} \cdot \boldsymbol{F}^{(1)} \, d\boldsymbol{v} = \boldsymbol{u} \otimes \boldsymbol{F}^{(1)} + \boldsymbol{F}^{(1)} \otimes \boldsymbol{u}, \tag{C20}$$

which leads to

$$\int \boldsymbol{v} \otimes \boldsymbol{v} f^{(1)} \, d\boldsymbol{v} = -\tau [P_0 (\boldsymbol{\nabla} \boldsymbol{u} + \boldsymbol{\nabla} \boldsymbol{u}^\dagger) + (\partial_t^{(1)} P_0 + \boldsymbol{\nabla} \cdot P_0 \boldsymbol{u}) \boldsymbol{I}], \tag{C21}$$

where the last two terms can be re-written as

$$\partial_t^{(1)} P_0 + \boldsymbol{\nabla} \cdot P_0 \boldsymbol{u} = \frac{\partial P_0}{\partial \rho} (\partial_t^{(1)} \rho + \boldsymbol{\nabla} \cdot \rho \boldsymbol{u}) + \left(P_0 - \rho \frac{\partial P_0}{\partial \rho} \right) \boldsymbol{\nabla} \cdot \boldsymbol{u}$$
$$= P_0 \left(1 - \frac{\partial \ln P_0}{\partial \ln \rho} \right) \boldsymbol{\nabla} \cdot \boldsymbol{u}, \tag{C22}$$

953 A4-41

in turn recovering the Navier–Stokes-level momentum equation:

$$\partial_t^{(2)} \rho \boldsymbol{u} - \nabla \cdot \mu \left(\nabla \boldsymbol{u} + \nabla \boldsymbol{u}^\dagger - \frac{2}{3} \nabla \cdot \boldsymbol{u} \boldsymbol{I} \right) - \nabla \cdot (\eta \nabla \cdot \boldsymbol{u} \boldsymbol{I}) = 0, \qquad (C23)$$

where

$$\mu = \tau P_0, \qquad (C24)$$

$$\eta = \tau P_0 \left(\frac{5}{3} - \frac{\partial \ln P_0}{\partial \ln \rho} \right). \qquad (C25)$$

Appendix D. Chapman–Enskog analysis of the lattice Boltzmann model

Using a Taylor expansion around $(\boldsymbol{r}, t)$,

$$f_i(\boldsymbol{r} + \boldsymbol{c}_i \delta t, t + \delta t) - f_i(\boldsymbol{r}, t) = \left[\delta t \mathcal{D}_t + \frac{\delta t^2}{2} \mathcal{D}_t^2 \right] f(\boldsymbol{r}, t) + O(\delta t^3), \qquad (D1)$$

the discrete time-evolution equation is re-written as

$$\delta t \mathcal{D}_t f_i + \frac{\delta t^2}{2} \mathcal{D}_t^2 f_i + O(\delta t^3) = \omega(f_i^{eq} - f_i) + (f_i^* - f_i^{eq}), \qquad (D2)$$

where we have only retained terms up to order two. Then, introducing characteristic flow size $\mathcal{L}$ and velocity $\mathcal{U}$, the equation is made non-dimensional as

$$\left(\frac{\delta r}{\mathcal{L}} \right) \mathcal{D}_t' f_i + \frac{1}{2} \left(\frac{\delta r}{\mathcal{L}} \right)^2 \mathcal{D}_t'^2 f_i = \omega(f_i^{eq} - f_i) + \left(f_i^*(\boldsymbol{u}' + \frac{\delta u}{\mathcal{U}} \delta \boldsymbol{u}') - f_i^{eq}(\boldsymbol{u}') \right), \qquad (D3)$$

where primed variables denote non-dimensional form and

$$\mathcal{D}_t' = \frac{\mathcal{U}}{c} (\partial_t' + \boldsymbol{c}_i' \cdot \nabla'), \qquad (D4)$$

where $c = \delta r / \delta t$. Assuming acoustic, i.e. $\mathcal{U}/c \sim 1$, and hydrodynamic, i.e. $\delta r / \mathcal{L} \sim \delta u / \mathcal{U} \sim \varepsilon$, scaling and dropping the primes for the sake of readability,

$$\varepsilon \mathcal{D}_t f_i + \frac{1}{2} \varepsilon^2 \mathcal{D}_t^2 f_i + O(\varepsilon^3) = \omega(f_i^{eq} - f_i) + (f_i^*(\boldsymbol{u} + \varepsilon \delta \boldsymbol{u}) - f_i^{eq}(\boldsymbol{u})). \qquad (D5)$$

Then introducing multi-scale expansions,

$$f_i = f_i^{(0)} + \varepsilon f_i^{(1)} + \varepsilon^2 f_i^{(2)} + O(\varepsilon^3), \qquad (D6)$$

$$f_i^* = f_i^{*(0)} + \varepsilon f_i^{*(1)} + \varepsilon^2 f_i^{*(2)} + O(\varepsilon^3), \qquad (D7)$$

the following equations are recovered at scales ε and ε^2:

$$\varepsilon : \mathcal{D}_t^{(1)} f_i^{(0)} = -\omega f_i^{(1)} + f^{*(1)}_i, \qquad (D8a)$$

$$\varepsilon^2 : \partial_t^{(2)} f_i^{(0)} + \mathcal{D}_t^{(1)} \left(1 - \frac{\omega}{2} \right) f_i^{(1)} = -\omega f_i^{(2)} + f^{*(2)}_i - \frac{1}{2} \mathcal{D}_t^{(1)} f^{*(1)}_i, \qquad (D8b)$$

with $f_i^{(0)} = f_i^{*(0)} = f_i^{eq}$. The moments of the non-local contributions (including both non-ideal contributions to the thermodynamic pressure, surface tension and the correction

953 A4-42

for the diagonals of the third-order moments tensor) are

$$\sum_i f^{*(k)}_i = 0, \quad \forall k > 0, \tag{D9a}$$

$$\sum_i c_i f^{*(1)}_i = F, \tag{D9b}$$

$$\sum_i c_i \otimes c_i f^{*(1)}_i = (u \otimes F + F \otimes u) + \Phi \tag{D9c}$$

$$\sum_i c_i \otimes c_i f^{*(2)}_i = \frac{1}{\rho} F \otimes F. \tag{D9d}$$

Taking the moments of the Chapman–Enskog-expanded equation at order ε,

$$\partial^{(1)}_t \rho + \nabla \cdot \rho u = 0, \tag{D10}$$

$$\partial^{(1)}_t \rho u + \nabla \cdot \rho u \otimes u + \nabla \cdot P_0 I + F = 0, \tag{D11}$$

while at order ε^2, the continuity equation is

$$\partial^{(2)}_t \rho + \nabla \cdot \frac{F}{2} = 0. \tag{D12}$$

Summing up (D10) and (D12), we recover the continuity equation as

$$\partial_t \rho + \nabla \cdot \rho U = 0, \tag{D13}$$

where $U = u + (\delta t / 2\rho) F$. For the momentum equations, we have

$$\partial^{(2)}_t \rho u + \frac{1}{2} \partial^{(1)}_t F + \frac{1}{2} \nabla \cdot (u \otimes F + F \otimes u) + \nabla \cdot \left(\frac{1}{2} - \frac{1}{\omega} \right) [\partial^{(1)}_t \Pi^{(0)}_2 + \nabla \cdot \Pi^{(0)}_3]$$

$$- \nabla \cdot \left(\frac{1}{2} - \frac{1}{\omega} \right) (u \otimes F + F \otimes u) + \nabla \cdot \frac{1}{\omega} \Phi = 0, \tag{D14}$$

where $\Pi^{(0)}_2$ and $\Pi^{(0)}_3$ are the second- and third-order moments of $f^{(0)}_i$ defined as

$$\Pi^{(0)}_2 = \rho u \otimes u + P_0 I, \tag{D15}$$

$$\Pi^{(0)}_3 = \Pi^{MB}_3 - \rho u \otimes u \otimes u \circ J - 3 \left(P_0 - \rho \varsigma^2 \right) u \otimes I \circ J \tag{D16}$$

where $\Pi^{MB}_{\alpha\beta\gamma} = \rho u_\alpha u_\beta u_\gamma + P_0 \, \mathrm{perm}(u_\alpha \delta_{\beta\gamma})$ is the third-order moment of the Maxwell–Boltzmann distribution, and for the sake of simplicity, we have introduced the diagonal rank three tensor J, with $J_{\alpha\beta\gamma} = \delta_{\alpha\beta} \delta_{\alpha\gamma} \delta_{\beta\gamma}$ and $\circ$ is the Hadamard product.

The contributions in the fourth term on the left-hand side can be expanded as

$$\partial_t^{(1)} \boldsymbol{\Pi}_2^{(0)} = \partial_t^{(1)} \rho \boldsymbol{u} \otimes \boldsymbol{u} + \partial_t^{(1)} P_0 \boldsymbol{I}$$

$$= \boldsymbol{u} \otimes \partial_t^{(1)} \rho \boldsymbol{u} + (\partial_t^{(1)} \rho \boldsymbol{u}) \otimes \boldsymbol{u} - \boldsymbol{u} \otimes \boldsymbol{u} \partial_t^{(1)} \rho + \partial_t^{(1)} P_0 \boldsymbol{I}$$

$$= -\boldsymbol{\nabla} \cdot \rho \boldsymbol{u} \otimes \boldsymbol{u} \otimes \boldsymbol{u} - [\boldsymbol{u} \otimes (\boldsymbol{\nabla} P_0 - \boldsymbol{F}) + (\boldsymbol{\nabla} P_0 - \boldsymbol{F}) \otimes \boldsymbol{u}] + \partial_t^{(1)} P_0 \boldsymbol{I} \quad \text{(D17)}$$

and

$$\boldsymbol{\nabla} \cdot \boldsymbol{\Pi}_3^{(0)} = \boldsymbol{\nabla} \cdot \rho \boldsymbol{u} \otimes \boldsymbol{u} \otimes \boldsymbol{u} + (\boldsymbol{\nabla} P_0 \boldsymbol{u} + \boldsymbol{\nabla} P_0 \boldsymbol{u}^\dagger) + (\boldsymbol{\nabla} \cdot P_0 \boldsymbol{u}) \boldsymbol{I}$$

$$- \boldsymbol{\nabla} \cdot [\rho \boldsymbol{u} \otimes \boldsymbol{u} \otimes \boldsymbol{u} \circ \boldsymbol{J} + 3 \left(P_0 - \rho \varsigma^2 \right) \boldsymbol{u} \otimes \boldsymbol{I} \circ \boldsymbol{J}], \quad \text{(D18)}$$

resulting in

$$\partial_t^{(1)} \boldsymbol{\Pi}_2^{(0)} + \boldsymbol{\nabla} \cdot \boldsymbol{\Pi}_3^{(0)} = P_0 (\boldsymbol{\nabla} \boldsymbol{u} + \boldsymbol{\nabla} \boldsymbol{u}^\dagger) + (\boldsymbol{u} \otimes \boldsymbol{F} + \boldsymbol{u} \otimes \boldsymbol{F}^\dagger)$$

$$+ (\boldsymbol{\nabla} \cdot P_0 \boldsymbol{u} + \partial_t^{(1)} P_0) \boldsymbol{I} - \boldsymbol{\nabla} \cdot [\rho \boldsymbol{u} \otimes \boldsymbol{u} \otimes \boldsymbol{u} \circ \boldsymbol{J} + 3 \left(P_0 - \rho \varsigma^2 \right) \boldsymbol{u} \otimes \boldsymbol{I} \circ \boldsymbol{J}]. \quad \text{(D19)}$$

Plugging this last equation back into (D14),

$$\partial_t^{(2)} \rho \boldsymbol{u} + \partial_t^{(1)} \frac{\boldsymbol{F}}{2} + \frac{1}{2} \boldsymbol{\nabla} \cdot (\boldsymbol{u} \otimes \boldsymbol{F} + \boldsymbol{F} \otimes \boldsymbol{u}) + \boldsymbol{\nabla} \cdot \left(\frac{1}{2} - \frac{1}{\omega} \right) P_0 (\boldsymbol{\nabla} \boldsymbol{u} + \boldsymbol{\nabla} \boldsymbol{u}^\dagger)$$

$$+ \boldsymbol{\nabla} \left(\frac{1}{2} - \frac{1}{\omega} \right) (\partial_t^{(1)} P_0 + \boldsymbol{\nabla} \cdot P_0 \boldsymbol{u})$$

$$+ \boldsymbol{\nabla} \cdot \left[\left(\frac{1}{2} - \frac{1}{\omega} \right) \boldsymbol{\nabla} \cdot (\rho \boldsymbol{u} \otimes \boldsymbol{u} \otimes \boldsymbol{u} \circ \boldsymbol{J} + 3 \left(P_0 - \rho \varsigma^2 \right) \boldsymbol{u} \otimes \boldsymbol{I} \circ \boldsymbol{J}) + \frac{1}{\omega} \boldsymbol{\Phi} \right] = 0, \quad \text{(D20)}$$

where the last term cancels out by setting

$$\boldsymbol{\Phi} = \left(1 - \frac{\omega}{2} \right) \boldsymbol{\nabla} \cdot (\rho \boldsymbol{u} \otimes \boldsymbol{u} \otimes \boldsymbol{u} \circ \boldsymbol{J} + 3 \left(P_0 - \rho \varsigma^2 \right) \boldsymbol{u} \otimes \boldsymbol{I} \circ \boldsymbol{J}), \quad \text{(D21)}$$

and the fourth and fifth terms reduce to the viscous stress tensor by defining $\mu / P_0 = (1/\omega - 1/2)$ and

$$P_0 \left(\frac{2 + D}{D} - \frac{\partial \ln P_0}{\partial \ln \rho} \right) \left(\frac{1}{\omega} - \frac{1}{2} \right) = \eta. \quad \text{(D22)}$$

Furthermore, using $\boldsymbol{U} = \boldsymbol{u} + (\delta t / 2\rho) \boldsymbol{F}$ and

$$\rho \boldsymbol{U} \otimes \boldsymbol{U} = \rho \boldsymbol{u} \otimes \boldsymbol{u} + \frac{\delta t}{2} (\boldsymbol{u} \otimes \boldsymbol{F} + \boldsymbol{F} \otimes \boldsymbol{u}) + \frac{\delta t^2 \boldsymbol{F} \otimes \boldsymbol{F}}{4\rho}, \quad \text{(D23)}$$

in combination with the Euler-level equation, and keeping in mind that errors of the form $\boldsymbol{\nabla} \cdot (\delta t^2 \boldsymbol{F} \otimes \boldsymbol{F}) / 4\rho$ in the convective term and $\delta t \boldsymbol{\nabla} \mu (\boldsymbol{\nabla} (\boldsymbol{F}/\rho) + \boldsymbol{\nabla} (\boldsymbol{F}/\rho)^\dagger)$ in the viscous stress are of order ε^3, one recovers

$$\partial_t \rho \boldsymbol{U} + \boldsymbol{\nabla} \cdot \rho \boldsymbol{U} \otimes \boldsymbol{U} - \boldsymbol{\nabla} \cdot \mu \left(\boldsymbol{\nabla} \boldsymbol{U} + \boldsymbol{\nabla} \boldsymbol{U}^\dagger - \frac{2}{D} \boldsymbol{\nabla} \cdot \boldsymbol{U} \boldsymbol{I} \right)$$

$$- \boldsymbol{\nabla} \cdot (\eta \boldsymbol{\nabla} \cdot \boldsymbol{U}) + O(\varepsilon^3) = 0. \quad \text{(D24)}$$

The scaling parameter introduced for the perturbation analysis, and consistency at the first two orders in ε, is further confirmed by simulations. To demonstrate this point, flat
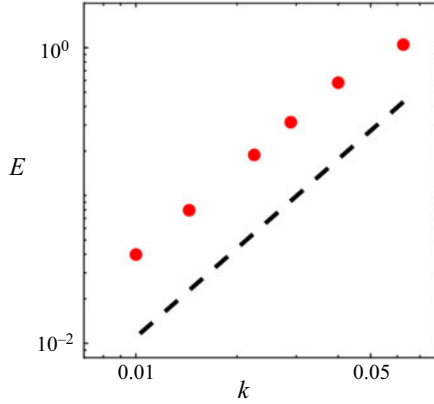
953 A4-44

Figure 28. Error in vapour-phase coexistence density, $E = |\rho_{v,ref} - \rho_{v,sim}|/\rho_{v,ref}$, as obtained from flat interface simulations (red circular markers). The dashed line shows the slope 2.

interface simulations at $T_r = 0.36$ have been conducted for different values of ε. The expansion parameter is controlled by introducing a scaling parameter k into the pressure P appearing inside the pseudo-potential, $P' = kP$, the reference pressure $P'_0 = kP_0$ and the surface tension term resulting in $F' = kF$. As introduced here, the scaling parameter directly scales the magnitude of the force term and therefore $k/\rho \sim \varepsilon$. It must be noted that this scaling is akin to a space grid refinement. The results obtained for different values of k are shown in figure 28 and point to a second-order scaling in agreement with the theoretical analysis provided in the manuscript.

Appendix E. Discrete non-local contributions to pressure tensor

Following the analysis presented by Shan (2008), we write the force contribution for the present model as

$$\boldsymbol{F} = \boldsymbol{F}^A + \boldsymbol{F}^B + \boldsymbol{F}^C + \boldsymbol{F}^D, \tag{E1}$$

$$\boldsymbol{F}^A = \pm \frac{8}{3}\psi(\boldsymbol{r}) \sum_{i=0}^{Q-1} \frac{w_i}{\varsigma^2} \boldsymbol{c}_i \psi(\boldsymbol{r} + \boldsymbol{c}_i \delta t), \tag{E2}$$

$$\boldsymbol{F}^B = \mp \frac{1}{3}\psi(\boldsymbol{r}) \sum_{i=0}^{Q-1} \frac{w_i}{\varsigma^2} \boldsymbol{c}_i \psi(\boldsymbol{r} + 2\boldsymbol{c}_i \delta t), \tag{E3}$$

$$\boldsymbol{F}^C = 2\tilde{\kappa}\rho(\boldsymbol{r}) \sum_{i=0}^{Q-1} \frac{w_i}{\varsigma^2} \boldsymbol{c}_i \rho(\boldsymbol{r} + \boldsymbol{c}_i \delta t), \tag{E4}$$

$$\boldsymbol{F}^D = -\tilde{\kappa}\rho(\boldsymbol{r}) \sum_{i=0}^{Q-1} \frac{w_i}{\varsigma^2} \boldsymbol{c}_i \rho(\boldsymbol{r} + 2\boldsymbol{c}_i \delta t). \tag{E5}$$
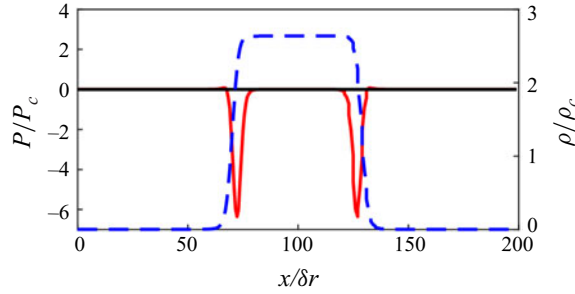
Figure 29. Pressure distribution from a simulation at $T_r = 0.36$, corresponding to $P_r = 0.0022$ and $\rho_l/\rho_v = 10^3$. Black line, evaluation using the discrete pressure tensor; red line, evaluation using continuous pressure tensor; dashed blue line, density profile.

The pressure tensor contributions from forces $\boldsymbol{F}^A$ and $\boldsymbol{F}^C$ can be readily written as

$$\boldsymbol{P}^A = \mp \frac{8}{6} \psi(\boldsymbol{r}) \sum_{i=0}^{Q-1} \frac{w_i}{\varsigma^2} \boldsymbol{c}_i \otimes \boldsymbol{c}_i \psi(\boldsymbol{r} + \boldsymbol{c}_i \delta t), \tag{E6}$$

$$\boldsymbol{P}^C = -\tilde{\kappa} \rho(\boldsymbol{r}) \sum_{i=0}^{Q-1} \frac{w_i}{\varsigma^2} \boldsymbol{c}_i \otimes \boldsymbol{c}_i \rho(\boldsymbol{r} + \boldsymbol{c}_i \delta t), \tag{E7}$$

while $\boldsymbol{F}^B$ and $\boldsymbol{F}^D$ contribute to the pressure tensor as follows:

$$\boldsymbol{P}^B = \pm \frac{1}{6} \left[\psi(\boldsymbol{r}) \sum_{i=0}^{Q-1} \frac{w_i}{\varsigma^2} \boldsymbol{c}_i \otimes \boldsymbol{c}_i \psi(\boldsymbol{r} + 2\boldsymbol{c}_i \delta t) + \sum_{i=0}^{Q-1} \frac{w_i}{\varsigma^2} \boldsymbol{c}_i \otimes \boldsymbol{c}_i \psi(\boldsymbol{r} - \boldsymbol{c}_i \delta t) \psi(\boldsymbol{r} + \boldsymbol{c}_i \delta t) \right], \tag{E8}$$

$$\boldsymbol{P}^D = \frac{\tilde{\kappa}}{2} \left[\rho(\boldsymbol{r}) \sum_{i=0}^{Q-1} \frac{w_i}{\varsigma^2} \boldsymbol{c}_i \otimes \boldsymbol{c}_i \rho(\boldsymbol{r} + 2\boldsymbol{c}_i \delta t) + \sum_{i=0}^{Q-1} \frac{w_i}{\varsigma^2} \boldsymbol{c}_i \otimes \boldsymbol{c}_i \rho(\boldsymbol{r} - \boldsymbol{c}_i \delta t) \rho(\boldsymbol{r} + \boldsymbol{c}_i \delta t) \right]. \tag{E9}$$

These expressions allow to compute the discrete pressure tensor with high accuracy. Figure 29 shows the distribution of the normal pressure, P_{xx}, in a flat interface simulation as computed from both the discrete and continuous pressure tensors,

$$P_{xx}^{cont} = P + \kappa (\partial_x^2 \rho - \tfrac{1}{2} |\partial_x \rho|^2). \tag{E10}$$

While the discrete evaluation method correctly results in a uniform pressure distribution throughout the domain, also across the interface, the continuous approximation evaluated using a finite differences approximation fails to do so, indicating errors due to higher-order terms. This points to the necessity of using the discrete pressure tensor instead of (E10) for evaluation of quantities such as surface tension and Tolman length in §§ 3.3 and 3.5.

953 A4-46

Appendix F. Analytical solution of layered Poiseuille flow

Solving the system presented in (4.1) and (4.2), one gets

$$u(y) = a_l y^2 + b_l y, \quad \forall y : 0 \le y \le h_l, \tag{F1a}$$

$$u(y) = a_v y^2 + b_v y + c_v, \quad \forall y : h_l \le y \le H, \tag{F1b}$$

with $a_l = -\rho_l g / 2\mu_l$, $a_v = -\rho_v g / 2\mu_v$, and

$$b_l = g \frac{H^2 \mu_l \rho_v - 2h_l^2 \mu_l \rho_l + h_l^2 \mu_l \rho_v + h_l^2 \mu_v \rho_l + 2Hh_l \mu_l \rho_l - 2Hh_l \mu_l \rho_v}{2\mu_l(H\mu_l - h_l\mu_l + h_l\mu_v)}, \tag{F2a}$$

$$b_v = g \frac{H^2 \mu_l \rho_v - h_l^2 \mu_l \rho_v + 2h_l^2 \mu_v \rho_v}{2\mu_v(H\mu_l - h_l\mu_l + h_l\mu_v)}, \tag{F2b}$$

$$c_v = gH \frac{h_l^2 \mu_l \rho_v + h_l^2 \mu_v \rho_l - 2h_l^2 \mu_v \rho_v - Hh_l \mu_l \rho_v + Hh_l \mu_v \rho_v}{2\mu_v(H\mu_l - h_l\mu_l + h_l\mu_v)}. \tag{F2c}$$

Appendix G. Isothermal sound speed for other equations of states

Apart from the van der Waals equation of state in the main text, the present LBM formulation was also used to simulate the speed of sound for the three other cubic equations of state, Peng–Robinson (3.4), Riedlich–Kwong–Soave (3.7) and Carnahan–Starling (3.10), along with two equations of state proposed by Shan & Chen (1993),

$$P_{SC} = P_0 + \frac{P_0 \mathcal{G}}{2} \psi_{SC}^2, \tag{G1}$$

with

$$\psi_{SC\text{-}I} = 1 - \exp(-\rho), \tag{G2}$$

$$\psi_{SC\text{-}II} = \exp(-1/\rho), \tag{G3}$$

while $P_0 = \varsigma^2 \rho$. Corresponding critical densities ρ_c and pseudo-temperatures $\mathcal{G}_c$ are readily computed by solving the conditions at the critical point,

$$\left.\frac{\partial P_{SC}}{\partial \rho}\right|_{\mathcal{G}_c, \rho_c} = 0, \quad \left.\frac{\partial^2 P_{SC}}{\partial \rho^2}\right|_{\mathcal{G}_c, \rho_c} = 0, \tag{G4a,b}$$

which results in ($\mathcal{G}_c = -4$, $\rho_c = 0.6931$) and ($\mathcal{G}_c = -7.389$, $\rho_c = 1$) for the pseudo-potentials (G2) and (G3), respectively. Figure 30 shows excellent agreement between simulations using the present model and theory for all equations of state. It is interesting to note that, in contrast to the conventional equations of state of the van der Waals type, the equations of state in (G1), (G2) and (G3) demonstrate higher speed of sound in the vapour phase than in the liquid. While this, by itself, does not contradict thermodynamics, it remains unclear which substances may feature such an unusual behaviour.

Appendix H. Alternative reference pressure

The general framework introduced in the present publication allows for a wide range of pressure partitions. As mentioned in the main text, one possible choice is to set $P_0 = P$ leaving only the surface tension contribution in (2.69). Another alternative is to follow the
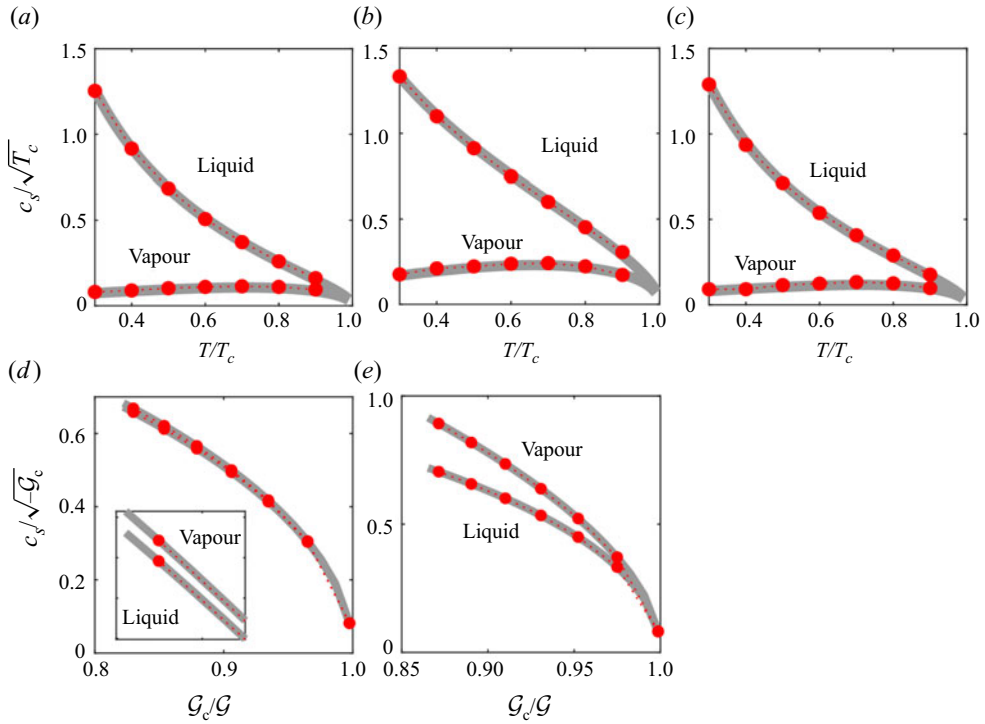
Figure 30. Isothermal sound speed for various equations of state. (*a–c*) Peng–Robinson (3.4), Carnahan–Starling (3.10) and Riedlich–Kwong–Soave (3.7); (*d,e*) Shan–Chen (G2) and (G3). Grey plain lines, theory; symbol, simulations with the present LB model.
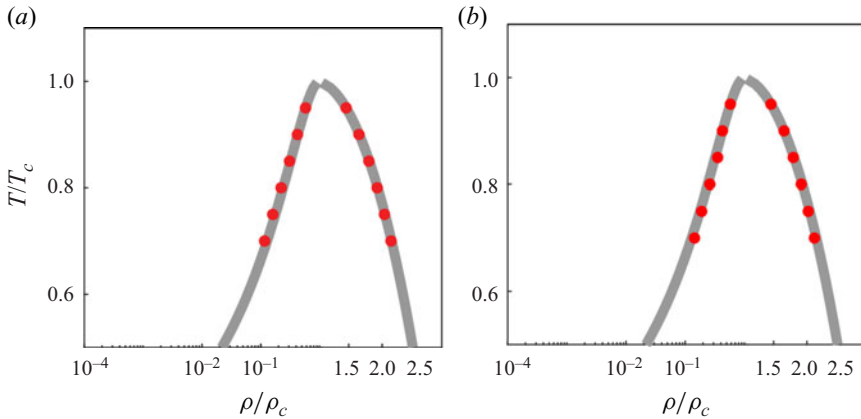

Figure 31. Liquid–vapour coexistence for the van der Waals equation of state using two different pressure partition choices: (*a*) using (H1) and (H2) ($a = 0.00033$, $b = 0.0952$) and (*b*) $P_0 = P$ ($a = 0.002$, $b = 0.381$). Grey lines, Maxwell's equal-area construction (3.1); red symbol, simulation.

Enkog–Vlasov short- and long-range interaction partition leading, for the van der Waals equation of state, to

$$P_0 = \frac{\rho RT}{1 - b\rho} \tag{H1}$$

and

$$P - P_0 = -a\rho^2. \tag{H2}$$

To better showcase the flexibility of the framework, flat interface simulations have been conducted using these alternative partitions. The resulting co-existence densities are shown in figure 31. For choices of partition leading to $P_0/\rho \neq$ const., an additional constraint tied to the stability properties of the chosen lattice must be taken into account. For instance, for standard lattices used in the present work, it is well known that $P_0 \delta t^2 / \rho \delta r^2 > 1/3$ would lead to instabilities. Simulations shown in figure 31 were run with parameters guaranteeing $P_0 \delta t^2 / \rho \delta r^2 < 1/3$.

REFERENCES

AALILIJA, A., GANDIN, C.-A. & HACHEM, E. 2020 On the analytical and numerical simulation of an oscillating drop in zero-gravity. *Comput. Fluids* **197**, 104362.

ANDERSON, D.M., MCFADDEN, G.B. & WHEELER, A.A. 1998 Diffuse-interface methods in fluid mechanics. *Annu. Rev. Fluid Mech.* **30** (1), 139–165.

BENZI, R., BIFERALE, L., SBRAGAGLIA, M., SUCCI, S. & TOSCHI, F. 2006 Mesoscopic modeling of a two-phase flow in the presence of boundaries: the contact angle. *Phys. Rev.* E **74** (2), 021509.

BLOKHUIS, E.M. & BEDEAUX, D. 1992 Pressure tensor of a spherical interface. *J. Chem. Phys.* **97** (5), 3576–3586.

BLOKHUIS, E.M. & KUIPERS, J. 2006 Thermodynamic expressions for the Tolman length. *J. Chem. Phys.* **124** (7), 074701.

BOUZIDI, M., FIRDAOUSS, M. & LALLEMAND, P. 2001 Momentum transfer of a Boltzmann-lattice fluid with boundaries. *Phys. Fluids* **13** (11), 3452–3459.

CAHN, J.W. & HILLIARD, J.E. 1958 Free energy of a nonuniform system. I. Interfacial free energy. *J. Chem. Phys.* **28** (2), 258–267.

CARNAHAN, N.F. & STARLING, K.E. 1969 Equation of state for nonattracting rigid spheres. *J. Chem. Phys.* **51** (2), 635–636.

CHAPMAN, S. & COWLING, T.G. 1939 *The Mathematical Theory of Non-uniform Gases: An Account of the Kinetic Theory of Viscosity, Thermal Conduction and Diffusion in Gases*. Cambridge University Press.

CHEN, L., KANG, Q., MU, Y., HE, Y.-L. & TAO, W.-Q. 2014 A critical review of the pseudopotential multiphase lattice Boltzmann model: methods and applications. *Intl J. Heat Mass Transfer* **76**, 210–236.

DEBENEDETTI, P.G. 1997 *Metastable Liquids*. Princeton University Press.

EGGERS, J., LISTER, J.R. & STONE, H.A. 1999 Coalescence of liquid drops. *J. Fluid Mech.* **401**, 293–310.

ENSKOG, D. 1921 Der Wärmeleitung, Reibung und Selbstdiffusion in gewissen verdichteten Gasen. *Kungl. Svenska Vetenskapsakademiens Handlingar.* **63** (4).

ESMAILI, E., MOOSAVI, A. & MAZLOOMI, A. 2012 The dynamics of wettability driven droplets in smooth and corrugated microchannels. *J. Stat. Mech.: Theory Exp.* **2012** (10), P10005.

GAUTHIER, A., SYMON, S., CLANET, C. & QUÉRÉ, D. 2015 Water impacting on superhydrophobic macrotextures. *Nat. Commun.* **6** (1), 8001.

GIBBS, J.W. 1874 On the equilibrium of heterogeneous substances. *Trans. Conn. Acad. Arts Sci.* **III**, 108–248.

GIOVANGIGLI, V. 2020 Kinetic derivation of diffuse-interface fluid models. *Phys. Rev.* E **102** (1), 012110.

GORBAN, A.N. & KARLIN, I.V. 2005 *Invariant Manifolds for Physical and Chemical Kinetics*, vol. 660. Springer.

GUGGENHEIM, E.A. 1945 The principle of corresponding states. *J. Chem. Phys.* **13** (7), 253–261.

HE, X. & DOOLEN, G.D. 2002 Thermodynamic foundations of kinetic theory and lattice Boltzmann models for multiphase flows. *J. Stat. Phys.* **107** (1), 309–328.

HE, X., SHAN, X. & DOOLEN, G.D. 1998 Discrete Boltzmann equation model for nonideal gases. *Phys. Rev.* E **57** (1), R13.

HELFRICH, W. 1978 Steric interaction of fluid membranes in multilayer systems. *Z. Naturforsch.* A **33** (3), 305–315.

HUANG, J., YIN, X. & KILLOUGH, J. 2019 Thermodynamic consistency of a pseudopotential lattice Boltzmann fluid with interface curvature. *Phys. Rev.* E **100** (5), 053304.

JAMET, D., LEBAIGUE, O., COUTRIS, N. & DELHAYE, J.M. 2001 The second gradient method for the direct numerical simulation of liquid–vapor flows with phase change. *J. Comput. Phys.* **169** (2), 624–651.

KARKHECK, J. & STELL, G. 1981 Kinetic mean-field theories. *J. Chem. Phys.* **75** (3), 1475–1487.

KIRKWOOD, J.G. & BUFF, F.P. 1949 The statistical mechanical theory of surface tension. *J. Chem. Phys.* **17** (3), 338–343.

KORTEWEG, D.J. 1901 Sur la forme que prennent les équations du mouvement des fluides si l'on tient compte des forces capillaires causées par des variations de densité considérables mais continues et sur la théeorie de la capillarité dans l'hypothese d'une variation continue de la densité. *Arch. Néerl. Sci. Exactes Nat* **6** (265).

KRÜGER, T., KUSUMAATMAJA, H., KUZMIN, A., SHARDT, O., SILVA, G. & VIGGEN, E.M. 2017 *The Lattice Boltzmann Method: Principles and Practice*, Graduate Texts in Physics, vol. 3. Springer International Publishing.

KUPERSHTOKH, A.L., MEDVEDEV, D.A. & KARPOV, D.I. 2009 On equations of state in a lattice Boltzmann method. *Comput. Maths Applics.* **58** (5), 965–974.

LAX, P.D. & RICHTMYER, R.D. 1956 Survey of the stability of linear finite difference equations. *Commun. Pure Appl. Maths* **9** (2), 267–293.

LI, Q., LUO, K.H., KANG, Q.J. & CHEN, Q. 2014 Contact angles in the pseudopotential lattice Boltzmann modeling of wetting. *Phys. Rev.* E **90** (5), 053301.

LI, Q., LUO, K.H., KANG, Q.J., HE, Y.L., CHEN, Q. & LIU, Q. 2016 Lattice Boltzmann methods for multiphase flow and phase-change heat transfer. *Prog. Energy Combust. Sci.* **52**, 62–105.

LI, Q., LUO, K.H. & LI, X.J. 2013 Lattice Boltzmann modeling of multiphase flows at large density ratio with an improved pseudopotential model. *Phys. Rev.* E **87** (5), 053301.

LIU, Y., MOEVIUS, L., XU, X., QIAN, T., YEOMANS, J.M. & WANG, Z. 2014 Pancake bouncing on superhydrophobic surfaces. *Nat. Phys.* **10** (7), 515–519.

LULLI, M., BIFERALE, L., FALCUCCI, G., SBRAGAGLIA, M. & SHAN, X. 2021 A mesoscale perspective on the Tolman length. *Phys. Rev.* E **105**, 015301.

LUO, K.H., FEI, L. & WANG, G. 2021 A unified lattice Boltzmann model and application to multiphase flows. *Phil. Trans. R. Soc.* A **379** (2208), 20200397.

MARTYS, N.S. 1999 Energy conserving discrete Boltzmann equation for nonideal systems. *Intl J. Mod. Phys.* C **10** (07), 1367–1382.

MARTYS, N.S. 2001 A classical kinetic theory approach to lattice Boltzmann simulation. *Intl J. Mod. Phys.* C **12** (08), 1169–1178.

MARTYS, N.S. 2006 A BBGKY-based density gradient approximation of interparticle forces: application for discrete Boltzmann methods. *Physica* A **362** (1), 57–61.

MAZLOOMI MOQADDAM, A., CHIKATAMARLA, S.S. & KARLIN, I.V. 2017 Drops bouncing off macro-textured superhydrophobic surfaces. *J. Fluid Mech.* **824**, 866–885.

MENCHACA-ROCHA, A., MARTÍNEZ-DÁVALOS, A., NÚÑEZ, R., POPINET, S. & ZALESKI, S. 2001 Coalescence of liquid drops by surface tension. *Phys. Rev.* E **63** (4), 046309.

PENG, D.-Y. & ROBINSON, D.B. 1976 A new two-constant equation of state. *Ind. Engng Chem. Fundam.* **15** (1), 59–64.

POPINET, S. 2018 Numerical models of surface tension. *Annu. Rev. Fluid Mech.* **50**, 49–75.

PROSPERETTI, A. & TRYGGVASON, G. 2009 *Computational Methods for Multiphase Flow*. Cambridge University Press.

RAO, M. & BERNE, B.J. 1979 On the location of surface of tension in the planar interface between liquid and vapour. *Mol. Phys.* **37** (2), 455–461.

RAYLEIGH, L. 1879 On the capillary phenomena of jets. *Proc. R. Soc. Lond.* **29** (196–199), 71–97.

REDLICH, O. & KWONG, J.N.S. 1949 On the thermodynamics of solutions. V. An equation of state. Fugacities of gaseous solutions. *Chem. Rev.* **44** (1), 233–244.

REYHANIAN, E., DORSCHNER, B. & KARLIN, I.V. 2020 Thermokinetic lattice Boltzmann model of nonideal fluids. *Phys. Rev.* E **102** (2), 020103.

SAADAT, M.H., HOSSEINI, S.A., DORSCHNER, B. & KARLIN, I.V. 2021 Extended lattice Boltzmann model for gas dynamics. *Phys. Fluids* **33** (4), 046104.

SBRAGAGLIA, M., BENZI, R., BIFERALE, L., SUCCI, S., SUGIYAMA, K. & TOSCHI, F. 2007 Generalized lattice Boltzmann method with multirange pseudopotential. *Phys. Rev.* E **75** (2), 026702.

SBRAGAGLIA, M., CHEN, H., SHAN, X. & SUCCI, S. 2009 Continuum free-energy formulation for a class of lattice Boltzmann multiphase models. *Europhys. Lett.* **86** (2), 24005.

SCARDOVELLI, R. & ZALESKI, S. 1999 Direct numerical simulation of free-surface and interfacial flow. *Annu. Rev. Fluid Mech.* **31** (1), 567–603.

SETHIAN, J.A. & SMEREKA, P. 2003 Level set methods for fluid interfaces. *Annu. Rev. Fluid Mech.* **35** (1), 341–372.

SHAN, X. 2008 Pressure tensor calculation in a class of nonideal gas lattice Boltzmann models. *Phys. Rev.* E **77** (6), 066702.

SHAN, X. & CHEN, H. 1993 Lattice Boltzmann model for simulating flows with multiple phases and components. *Phys. Rev.* E **47** (3), 1815–1819.

SOAVE, G. 1972 Equilibrium constants from a modified Redlich-Kwong equation of state. *Chem. Engng Sci.* **27** (6), 1197–1203.

STALDER, A.F., MELCHIOR, T., MÜLLER, M., SAGE, D., BLU, T. & UNSER, M. 2010 Low-bond axisymmetric drop shape analysis for surface tension and contact angle measurements of sessile drops. *Colloids Surf.* A **364** (1-3), 72–81.

SUCCI, S. 2002 *The Lattice Boltzmann Equation for Fluid Dynamics and Beyond*. Oxford Science Publications.

TOLMAN, R.C. 1949 The effect of droplet size on surface tension. *J. Chem. Phys.* **17** (3), 333–337.

VADILLO, D.C., SOUCEMARIANADIN, A., DELATTRE, C. & ROUX, D.C.D. 2009 Dynamic contact angle effects onto the maximum drop impact spreading on solid surfaces. *Phys. Fluids* **21** (12), 122002.

VAN BEIJEREN, H. & ERNST, M.H. 1973 The modified Enskog equation. *Physica* **68** (3), 437–456.

VLASOV, A.A. 1961 *Many-particle Theory and its Application to Plasma*. Gordon & Breach Science Publisher Inc.

VAN DER WAALS, J.D. 1873 Over de Continuiteit van den Gasen Vloeistoftoestand. PhD thesis, University of Leiden.

VAN DER WAALS, J.D. 1894 Thermodynamische Theorie der Kapillarität unter Voraussetzung stetiger Dichteänderung. *Z. Phys. Chem.* **13U** (1).

WIDOM, B. 1965 Surface tension and molecular correlations near the critical point. *J. Chem. Phys.* **43** (11), 3892–3897.

YUAN, P. & SCHAEFER, L. 2006 Equations of state in a lattice Boltzmann model. *Phys. Fluids* **18** (4), 042101.